communications chemistry

Review article

https://doi.org/10.1038/s42004-024-01389-8

Phase relations of bridgmanite, the most abundant mineral in the Earth's lower mantle

Check for updates

Tomoo Katsura

The knowledge of phase relations of constitutive minerals is essential to investigate the structure, dynamics and evolution of the Earth and planetary interiors. This paper reviews the phase relations of bridgmanite, the most abundant mineral in the Earth's lower mantle, with an ideal composition of $MgSiO_3$. Bridgmanite has an orthorhombic structure with larger dodecahedral A and smaller octahedral B cation sites. The A-sites can incorporate Mg^{2+}, Fe^{2+}, Fe^{3+}, and Al^{3+}, while the B-sites accommodate Si^{4+}, Al^{3+} and Fe^{3+}. The incorporation of hydrogen and large cations like Ca is likely limited, although these issues are still debated. Al^{3+} and Fe^{3+}, respectively, can form the charge-coupled components, $AlAlO_3$ and $Fe^{3+}Fe^{3+}O_3$ occupying both A- and B-sites. When both Al^{3+} and Fe^{3+} are present, Al^{3+} occupies B-sites, and Fe^{3+} occupies A-sites, forming $Fe^{3+}AlO_3$. In systems with excess MgO, Al and Fe^{3+} also form the oxygen vacancy components $MgAl^{3+}O_{2.5}\square_{0.5}$ and $MgFe^{3+}O_{2.5}\square_{0.5}$. The phase relationships of bridgmanite with coexisting phases are discussed as a function of pressure, temperature, and oxygen fugacity from the simple $MgSiO_3$ system to the complex MgO-Fe^{2+}O-$Fe^{3+}{}_2O_3$-Al_2O_3-SiO_2 system.

Bridgmanite ((Mg, Fe)SiO_3-Al_2O_3, Bdm) is the Earth's lower mantle's most abundant mineral. The lower mantle extends from 660 Km to 2890 Km depth, corresponding to 23–136 GPa, and comprises 56% of Earth's volume. The mantle's composition is primarily peridotitic, containing 45.0% SiO_2, 37.8% MgO, 8.1% Fe_xO, 3.6% CaO, and 4.45% Al_2O_3 by weight[1]. The lower mantle's mineralogy consists of 80% Bdm, 15% ferropericlase ((Mg, Fe)O, Fper), and 10% of davemaoite ($CaSiO_3$, Dvm) by volume (Fig. 1A)[2]. Below the D" discontinuity in high-velocity regions, postperovskite ((Mg, Fe)SiO_3-Al_2O_3) likely replaces Bdm[3]. The differentiation under mid-oceanic ridges creates oceanic plates with 18% basalt and 82% harzburgite[2], which subduct into the lower mantle. The resulting basaltic domain contains 32% Bdm, 25% Dvm, 26% postspinel phase ($MgAl_2O_4$, PS), and 18% stishovite (SiO_2, Sti) (Fig. 1B), while the harzburgite domain comprises 74% Bdm, 22% Fper, and 3% Dvm (Fig. 1C)[2]. As the predominant mineral in all lithologies of the lower mantle, Bdm's phase relations with secondary minerals, *i.e.*, Fper, Dvm, PS, and Sti, are crucial for understanding mantle dynamics and evolution. Bdm is named after Percy Williams Bridgman, a pioneering American high-pressure physicist.

This review examines Bdm's phase relations with secondary phases under pressure (P)—temperature (T) conditions relevant to Earth's mantle. It focuses on major mantle elements (O, Si, Mg, Fe, Al, and Ca) and H, which, although not a major constituent, could significantly alter mineral properties[4]. This study excludes phase relations in natural systems. Figure 1 illustrates Bdm's predominance in the lower mantle but does not specify exact mineral proportions.

Bdm phase relations are primarily studied using laser-heated diamond anvil cells (LH-DAC) and multi-anvil presses (MAP). LH-DAC covers Bdm's entire stability field but has significant temperature uncertainties (100–400 K)[5–11] and pressure uncertainties (1–5 GPa or up to 7%)[6,7,9–12]. It also risks chemical heterogeneity due to the Soret effect[13]. Sample analysis techniques have evolved from unit cell volume estimates to transmission electron microscopy (TEM) with focused ion beam (FIB), though spatial resolution remains a challenge for very small grain sizes. Notably, silicate samples prepared using FIB are typically more than 100 nm, and the spatial resolution of TEM analysis is comparable to the sample thickness[14]. On the other hand, MAP offers more precise P-T conditions, with temperature fluctuations of typically 5 K[15–18] and pressure uncertainties of 0.05–1 GPa[15–19]. It avoids Soret effect issues. The size of recovered samples is several hundred μm, allowing various post-analysis using multiple techniques. The phases present can be identified using a microfocused powder X-ray diffractometer (MF-XRD). Sample textures can be observed using scanning electron microscopy (SEM) with backscattered electron imaging (BEI). The grain sizes are larger than 2-3 μm below 27 GPa and above 1700 K, allowing for reliable compositional analysis using an electron microprobe (EPMA), whose precision is better than 0.1 wt.%[20–26]. The grain size becomes smaller with increasing pressure but usually above several

Bayerisches Geoinstitut, University of Bayreuth, Bayreuth, Germany. e-mail: tomo.katsura@uni-bayreuth.de

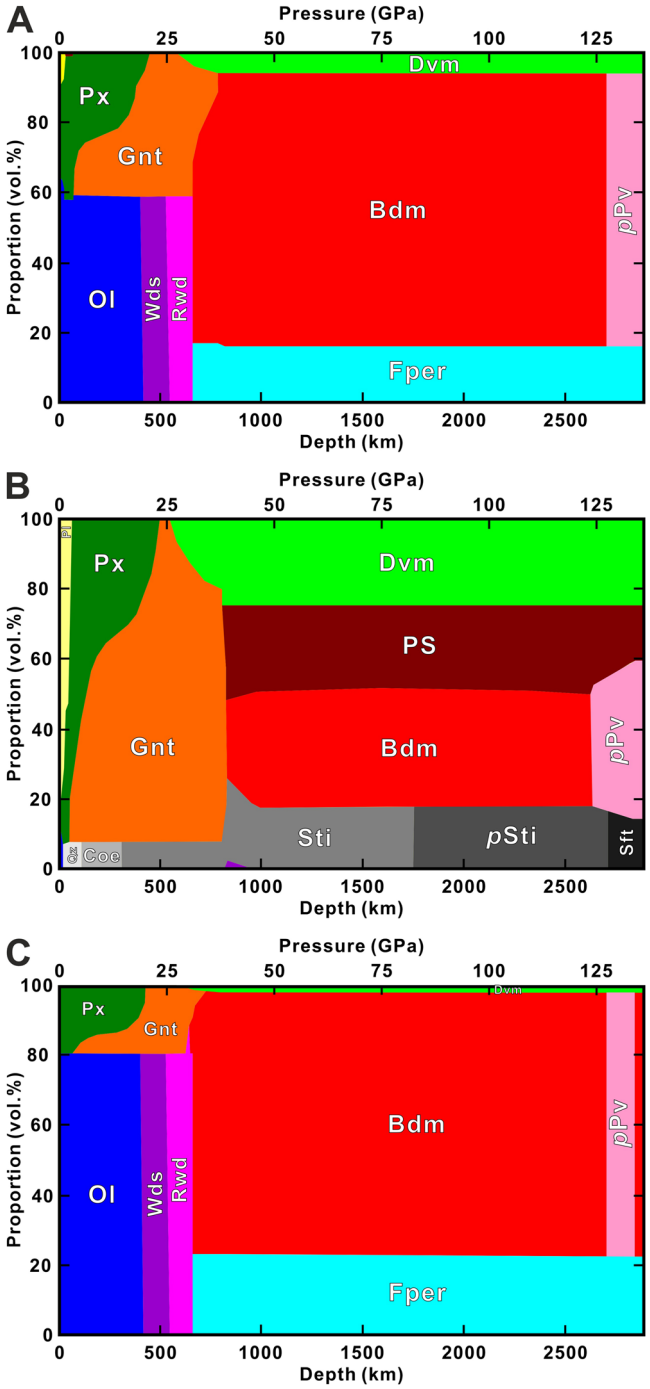

Fig. 1 | Mineral constitution of mantle rocks. A Pyrolite, **B** basalt, **C** harzburgite. Mineral abbreviation: Bdm (red), bridgmanite; Fper (cyan), ferropericlase; Dvm (light green), davemaoite: *p*Pv (pink), postperovskite; Ol (blue), olivine ((Mg, Fe)$_2$SiO$_4$); Wds (blue-violet), wadsleyite ((Mg, Fe)$_2$SiO$_4$); Rwd (magenta), ringwoodite ((Mg, Fe)$_2$SiO$_4$); Gnt (orange), garnet ((Mg, Fe, Ca)SiO$_3$-Al$_2$O$_3$); Px, pyroxenes (dark green); Pl (yellow), plagioclase; PS (dark red): postspinel phase (CaFe$_2$O$_4$-type MgAl$_2$O$_4$), Qz (very light grey): quartz (SiO$_2$), Coe (light grey): coesite (SiO$_2$), Sti (gray): stishovite (SiO$_2$), *p*Sti (dark gray): post-stishovite (CaCl$_2$-type SiO$_2$), Sft (very dark gray): seifertite (α-PbO$_2$ type SiO$_2$). Modified from Strixrude and Lithgow-Bertelloni[2].

100 nm, which allows reliable analysis using an analytical TEM with an energy-dispersive X-ray spectrometer (EDS). The determination of $Fe^{3+}/\Sigma Fe$ is also possible using Mössbauer spectroscopy with a precision of 0.02 ~ 0.05[25–30]. MAP's pressure range was historically limited to 26 GPa but recently extended to 52 GPa[31]. This paper reviews the experimental data obtained using MAP and LH-DAC, supplemented by ab initio calculations.

Crystal chemistry of bridgmanite

Bdm has an orthorhombic perovskite structure (Fig. 2A)[32,33] with MgSiO$_3$ as its principal component. In this structure, Mg^{2+} and Si^{4+} occupy the A- and B-sites, respectively, surrounded by eight~twelve and six O^{2-} [33], expressed as $[Mg^{2+}]_A[Si^{4+}]_BO_3^{2-}$. Dvm also has a perovskite structure, but in cubic form[34] (Fig. 2B). This difference between Bdm and Dvm is due to the ionic radii of their A-site cations: 8-coordinated Mg^{2+} (89 pm) and Ca^{2+} (112 pm), respectively[35,36]. The smaller Mg^{2+} in Bdm causes A-site distortion and SiO$_6$ octahedron rotation, resulting in the orthorhombic structure. In contrast, the larger Ca^{2+} in Dvm allows for the cubic perovskite structure.

Ionic radii of cations provide insights into Bdm chemistry. The A-site, typically occupied by 8-coordinated Mg^{2+}, can accommodate similarly sized cations like Fe^{2+} (92 pm) and Fe^{3+} (78 pm) in high-spin states. It doesn't primarily accommodate larger cations like Ca^{2+}. Al^{3+} (estimated 61 pm) can occupy the A-site[37], but its smaller size may explain why high pressure is needed for incorporation. The B-site, occupied by 6-coordinated Si^{4+} (40 pm), can only accommodate small cations. Al^{3+} (54 pm) fits well, while Fe^{3+} (66 pm) is accommodated in limited amounts[20], possibly due to its larger size. The 6-coordinated ionic radius of high-spin Fe^{2+} (78 pm) is likely too large for the B-site. Note: Effective ionic radii were extrapolated from Shannon's[36] data when not explicitly given.

The valence differences between Mg^{2+} and Si^{4+} (2+ and 4+ valence) and Al^{3+} and Fe^{3+} (3+ valence) lead to various substitution mechanisms in Bdm. When Al or Fe^{3+} occupies the A- or B-site, it is favourable for the other site to also be occupied by a trivalent cation, forming charge-coupled (CC) components like $[Al^{3+}]_A[Al^{3+}]_BO^{2-}{}_3$ and $[Fe^{3+}]_A[Fe^{3+}]_BO^{2-}{}_3$[20,37]. However, as the ionic radii of Al and Fe^{3+} are more similar to those of Si and Mg, respectively, the Fe^{3+} and Al cations are preferably accommodated in the A- and B-sites, respectively, forming $[Fe^{3+}]_A[Al^{3+}]_BO^{2-}{}_3$[21]. Al and Fe^{3+} can also occupy the B-site even when divalent cations (Mg^{2+} and Fe^{2+}) are in the A-site. This creates oxygen vacancies (□) to balance charges, forming oxygen vacancy (OV) components like $[Mg^{2+}]_A[Al^{3+}]_BO^{2-}{}_{2.5}\square_{0.5}$ and $[Fe^{2+}]_A[Al^{3+}]_BO^{2-}{}_{2.5}\square_{0.5}$[38]. Conversely, when Al or Fe^{3+} occupies the A site with Si^{4+} in the B site, cation vacancies form to compensate for excess positive charge, resulting in A-site vacancy (AV) components like $[\square_{1/3}Al^{3+}{}_{2/3}]_A[Si^{4+}]_BO^{2-}{}_3$ and $[\square_{1/3}Fe^{3+}{}_{2/3}]_A[Si^{4+}]_BO^{2-}{}_3$[20,38].

Molar volume is crucial for understanding chemical changes with *P*. Table 1 shows molar volumes of various Bdm components at ambient conditions. All secondary components have larger molar volumes than MgSiO$_3$ (24.447(4) cm^3/mol), including OV, despite their lack of oxygen.

The incorporation mechanism of H^+ in Bdm is not yet fully understood until recently due to the limited H$_2$O content. Drawing parallels from Mg$_2$SiO$_4$ wadsleyite, an upper mantle mineral, where H^+ occupies the Mg site forming the $[Mg^{2+}2H^+]_2[Si^{4+}]O^{2-}{}_4$[39], it was hypothesised that H^+ might similarly occupy the Mg (A-) site in Bdm[40], creating $[2H^+]_A[Si^{4+}]_BO^{2-}{}_3$. An alternative mechanism proposed that H^+ could couple with Al^{3+} to substitute Si^{4+} in the B-site[41], forming $[Mg^{2+}]_A[Al^{3+}H^+]_BO^{2-}{}_3$ A recent neutron scattering study has provided evidence supporting this latter substitution mechanism in Bdm[42].

The variety of components in Bdm underscores the importance of coexisting phases in determining its chemistry. The species of coexisting phases should vary with the bulk composition. The content of different components in Bdm varies with the coexisting phases, which in turn depend on the bulk composition. In (Mg, Fe^{2+})O excess or SiO$_2$-deficient systems, OV likely forms, while in SiO$_2$ excess systems, AV forms[38]. To define a unique defect structure at a given *P* and *T*, the Gibbs phase rule must be considered. For a system with *n* components, *n-1* additional phases must coexist with Bdm. For instance, in a three-component system (MgO-Al$_2$O$_3$-SiO$_2$), two additional phases besides Bdm are necessary. Many studies have not fully considered the implication of the phase rule, often having an insufficient number of coexisting phases. While the following sections will

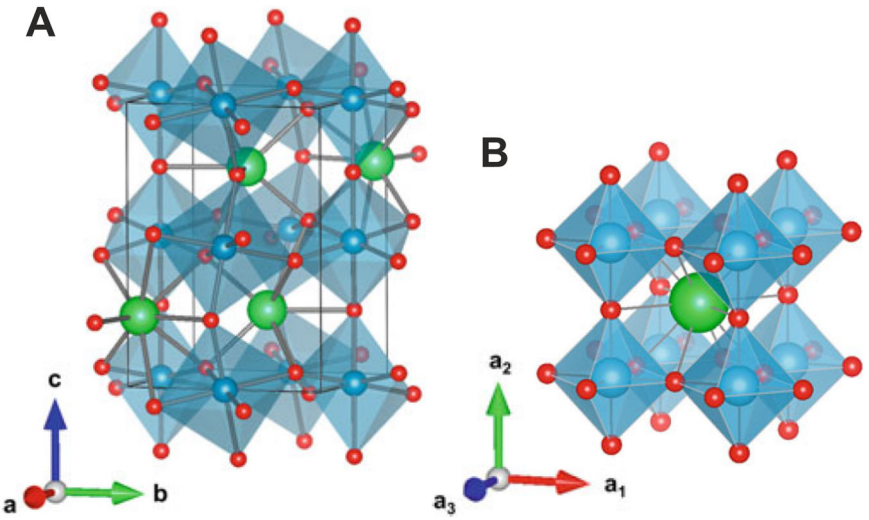

Fig. 2 | Perovskite structures. A orthorhombic perovskite structure, **B** cubic perovskite structure. The **A** and **B** site cations and oxygen, respectively, are expressed using green, blue, and red spheres. Modified from Akaogi[35].

interpret Bdm phase relations, it is important to note that this review is not exhaustive.

Phase relations of bridgmanite in various systems

$MgSiO_3$. The $MgSiO_3$ system is fundamental for understanding Bdm stability. Figure 3 summarises Bdm's stability field, bounded by transitions to akimotoite (Aki) at low P and T [43–51], to postperovskite (pPv) at high P[5,52–55], and $MgSiO_3$ melt at high T [56–64]. A small region of tetragonal garnet (Gnt), often referred to as majorite, exists between Aki and melt[47,56]. Recent studies define these boundaries with more precision. Figure 3 shows the most recently determined boundaries with Aki[49], pPv[5], and melt[64]. The Bdm- Aki boundary has a negative slope (dP/dT), −3.2 to −8.1 $MPaK^{-1}$ as T decreases from 2100 to 1250 K[49] with transition P at 24.0 GPa at 2100 K and 20.5 GPa at 1250 K. The Bdm-pPv boundary exhibits a steep positive dP/dT of 13.3 $MPaK^{-1}$, with transition P at 107 GPa at 1500 K and 150 GPa at 4500 K[35]. The melting curve starts at 2700 ~ 2800 K at 22 GPa[56,63], rapidly increases to 4300 K at 60 GPa, then gradually reaches 5200 K at 140 GPa[64]. Extrapolation suggests a triple point (Bdm-pPv-melt) at 5200 K and 160 GPa. The Bdm-Gnt boundary remains less studied.

Table 1 | Molar volumes of mineral components at ambient conditions

Mineral	Components	Molar volume ($cm^3\ mol^{-1}$)
Bridgmanite	$MgSiO_3$	24.47(1)[a]
	$Fe^{2+}SiO_3$	25.35(2)[b]
	$AlAlO_3$	25.84(3)[c]
	$MgAlO_{2.5}\square_{0.5}$	26.64(10)[d]
	$Fe^{3+}Fe^{3+}O_3$	29.55(3)[e]
	$MgFe^{3+}O_{2.5}\square_{0.5}$	27.65(1)[e]
	$Fe^{3+}AlO_3$	27.09(6)[e]
Corundum	$AlAlO_3$	25.64(1)[c]
	$MgSiO_3$	26.06(9)[c]
Akimotoite	$MgSiO_3$	26.46(1)[d]
Ferropericlase	MgO	11.25[e]
	FeO	12.26[e]
Post-spinel phase	$MgAl_2O_4$	36.14(1)[f]
	Mg_2SiO_4	36.49(2)[f]

There are no data about pPv or Dvm due to their unquenchability.
[a]Horiuch et al.[33]; [b]Kudo et al.[73]; [c]Liu et al.[114]; [d]Liu et al.[119]; [e]Huang et al.[125], [f]Kojitani et al.[113].

MgO-SiO_2. In the MgO-rich region of the MgO-SiO_2 system, Bdm coexists with periclase (MgO, Per). The Bdm+Per field is bounded by ringwoodite (Mg_2SiO_4, Rwd) at low-P, as shown in Fig. 4A. This phase boundary, extensively studied for its geophysical importance in relation to the 660-km seismic discontinuity, occurs at 23–24 GPa[15,31,43,49,65–67]. The Rwd to Bdm + Per transition exhibits a near-zero dP/dT below 1700 K, becoming increasingly negative at higher T, reaching −0.9 $MPaK^{-1}$ at 2000 K[68]. Above 2500 K, Rwd transforms into wadsleyite (Mg_2SiO_4, Wds) following a boundary 11.0 (GPa) + 4.5 ($MPaK^{-1}$) × T (K)[68], leading to a transition from Bdm + Per to Wds rather than Rwd. Both Bdm + Per and Wds become melt + Per above 2500 K at 19 to 27 GPa[63].

On the SiO_2-rich region of the MgO-SiO_2 system, Bdm coexists with SiO_2 stishovite (Sti) at a relatively lower P. At 68-78 GPa, Sti transforms to $CaCl_2$-type SiO_2, known as post-stishovite (pSt)[6]. At even higher P, pSt may transform to α-PbO_2-type SiO_2, called seifertite (Sft), although it is unclear if this transformation occurs within the Bdm stability field[7]. Thus, above 68-78 GPa, Bdm primarily coexists with pSt. No intermediate phases between Bdm and silica phases have been reported in the literature.

The melting relations of Bdm + Per and Bdm + Sti, though not extensively studied, exhibit congruent melting[69]. Figure 4B illustrates the melting relations in the MgO-SiO_2 system proposed by Yao et al.[69] based on multi-anvil experiments and first-principle calculations. At 24 GPa, the eutectic T for Bdm + Per and Bdm + Sti, respectively, are 2650 K[63] and 2700 K[69]. Per and Sti have significantly higher melting T (4800 and 4200 K) than Bdm (2750 K) at this P. Consequently, the compositions of Bdm + Per and Bdm + Sti melts are similar to pure Bdm with $MgO/(MgO+SiO_2)$ of 0.43 and 0.53, respectively, compared to 0.5 for Bdm. As P increases, the melting T in the MgO-SiO_2 system rises while maintaining similar geometrical relations. At 136 GPa, the eutectic T for Bdm + Per and Bdm + Sti reaches 5500 and 5400 K, respectively. As the melting temperature differences between Bdm (5550 K) and Per (7500 K) and Sti (5900 K) decrease, the eutectic compositions of Bdm + Per and Bdm + Sti, $MgO/(MgO+SiO_2)$ = 0.35 and 0.67, respectively, deviate more significantly from the $MgSiO_3$ composition.

MgO-$Fe^{2+}O$-SiO_2. Following the MgO-SiO_2 system, the MgO-$Fe^{2+}O$-SiO_2 system was initially anticipated to be the second most important system in geophysics due to Fe's abundance as the fourth element in Earth's mantle[1]. While the majority of Earth's Fe is stored in the liquid outer core, the deep mantle's reducing conditions[70] led to the expectations that Fe would primarily exist in its 2+ state. However, recent studies have revealed that Fe^{3+} plays an even more crucial role in mantle chemistry than Fe^{2+} [27,71], a topic that will be explored in later sections. The investigation of Bdm's phase relations in this system began shortly after

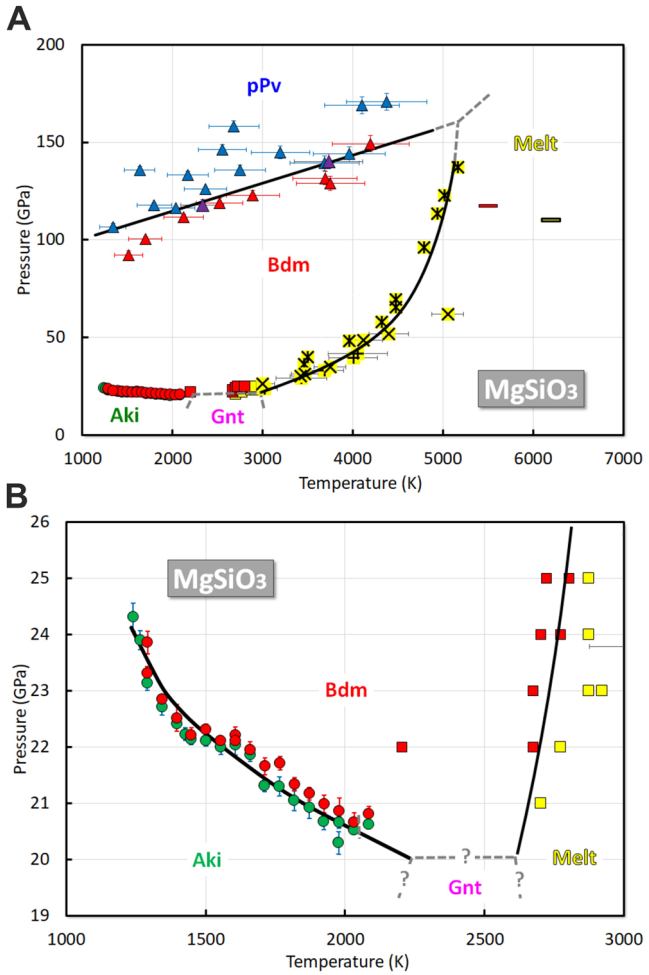

Fig. 3 | Stability of Bdm in pure $MgSiO_3$. A at 1000 to 7000 K and 0 to 200 GPa, and **B** at 1000–3000 K and 19–26 GPa. Colour code: Red–Bdm, Green - Aki, Purple - Gnt, Blue - *p*Pv, Yellow - Melt. Data sources: Circles - Chanysheve et al.[49], Triangles - Tateno et al.[5], Squares - Ito and Katsura[56], Stars - Shen and Lazor[58], Crosses - Zerr and Boehler[59], Plus sings - Akins et al.[59].

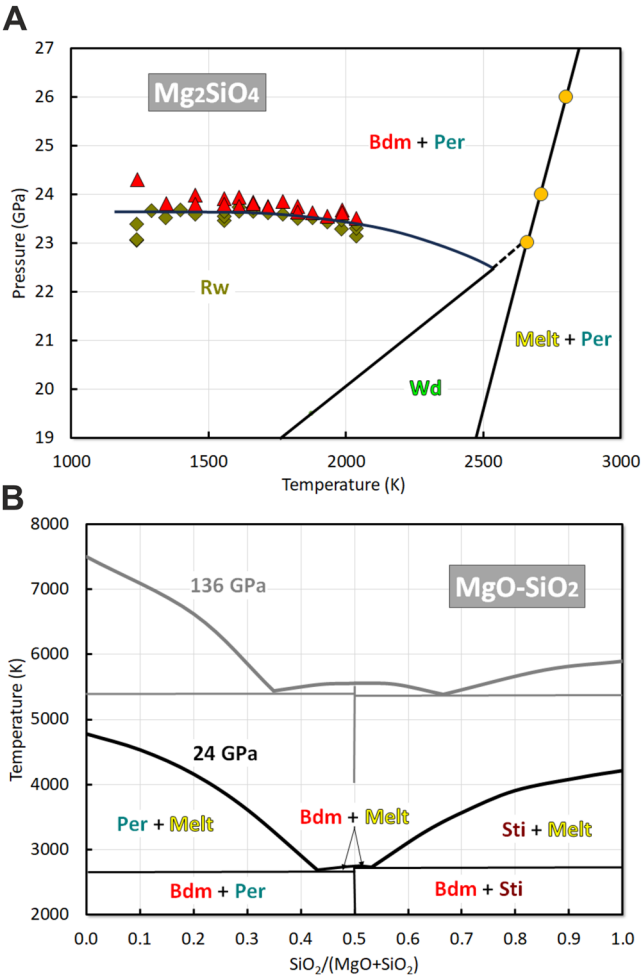

Fig. 4 | Stability of Bdm in MgO-SiO_2. A Phase relations in Mg_2SiO_4 system at 19–27 GPa and 1000–3000 K. Red: Bdm, marron: Rwd, light green: Wds, blue-green: Per, yellow: melt. Triangles and diamonds: Chanyshev et al.[49], circle: Liebske and Frost[63]. The boundary between Rwd and Wds is the extrapolation of Tsujino et al.[68]. **B** Melting relations in Mg_2SiO_4 at 24 and 136 GPa and 2000–8000 K. Modified from Yao et al.[69].

its discovery[72], reflecting its perceived importance in understanding Earth's lower mantle composition and dynamics.

Maximum $Fe^{2+}SiO_3$ content. Fe^{2+} can substitute for Mg^{2+} in the A-site, forming $Fe^{2+}SiO_3$[73]. However, there is a limit to the maximum $Fe^{2+}SiO_3$ content in Bdm, denoted as $\varphi^{Bdm}_{Fe^{2+}SiO_3}$. When the $Fe^{2+}SiO_3$ content in Bdm, $\chi^{Bdm}_{Fe^{2+}SiO_3}$, exceeds this limit, Fper + Sti forms. In planets with mantles richer in $Fe^{2+}O$ than Earth's, Fper + Sti could be the major mantle phase rather than Bdm. Due to its geophysical significance, $\varphi^{Bdm}_{Fe^{2+}SiO_3}$ has been extensively studied as a function of T [43,75–77] and P [8,76–78]. While Fe^{2+} undergoes a spin transition in certain minerals like Fper, at high P[79], Fe^{2+} in the Bdm A-site remains in the high-spin state throughout its stability field[79]. Consequently, the chemistry of Fe^{2+}-bearing Bdm should change gradually or remain unaltered with P.

Figure 5A illustrates the variation of $\varphi^{Bdm}_{Fe^{2+}SiO_3}$ at *ca.* 26 GPa as a function of T determined using a MAP[43,75–77]. The data can be divided into two groups based on the anvil material: tungsten carbide (WC)[43,74,75] and sintered diamond (SD)[76,77]. Studies using WC anvils found $\varphi^{Bdm}_{Fe^{2+}SiO_3}$ to be 7 mol.% at 1400 K, increasing to 12 mol.% at 2000 K. In contrast, studies using SD anvils reported 16 mol.% at 1800 K, rising to to 18 mol.% at 2300 K. The SD anvils results are 1.3-2.0 times higher than WC anvil results at comparable T. The reason for this discrepancy is not fully understood. One possible explanation is that the actual T in the WC anvil experiments may have been higher than that in the SD anvil experiments, though this would require a difference of over 1000 K to account for this difference in $\varphi^{Bdm}_{Fe^{2+}SiO_3}$. Another possibility is that extremely small grain sizes in the SD anvil experiments may have led to microprobe analyses of bridgmanite inadvertently including more Fe-rich ferropericlase grains.

Figure 5B illustrates the variation in $\varphi^{Bdm}_{Fe^{2+}SiO_3}$ as a function of P at various T using data from LH-DAC experiments[8,78] and MAP with SD anvils[76,77]. Both data indicate that $\varphi^{Bdm}_{Fe^{2+}SiO_3}$ increases with P at similar rates of 0.42 to 0.60 mol.%GPa^{-1} with no apparent effect from the Fe^{2+} spin transition in Fper[79]. LH-DAC results show lower $\varphi^{Bdm}_{Fe^{2+}SiO_3}$[8,78] compared to MAP with SD anvils[76,77], but are consistent with MAP using WC anvils[43,74,75]. MAP with SD anvils[76,77] yielded a $\varphi^{Bdm}_{Fe^{2+}SiO_3}$ of 38 mol.% at 2000 K near 60 GPa. Dorfman et al.'s LH-DAC study on the $MgSiO_3$-$Fe^{2+}SiO_3$ system[8] showed a rapid increase in $\varphi^{Bdm}_{Fe^{2+}SiO_3}$ from 60 to 70 GPa, implying a possible formation of pure $Fe^{2+}SiO_3$ Bdm. However, this drastic change is challenging to interpret thermodynamically without assuming significant changes in partial molar volumes with increasing P. The Sti-*p*Sti transition occurring between 58 and 78 GPa has minimal effect on phase relations due to similar volumes of these minerals[6].

Given the inconsistencies in the reported $\varphi^{Bdm}_{Fe^{2+}SiO_3}$, a comprehensive reinvestigation is necessary. This study should cover a wide P-T range and employ reliable experimental and analytical techniques to establish more definitive conclusions about $\varphi^{Bdm}_{Fe^{2+}SiO_3}$.

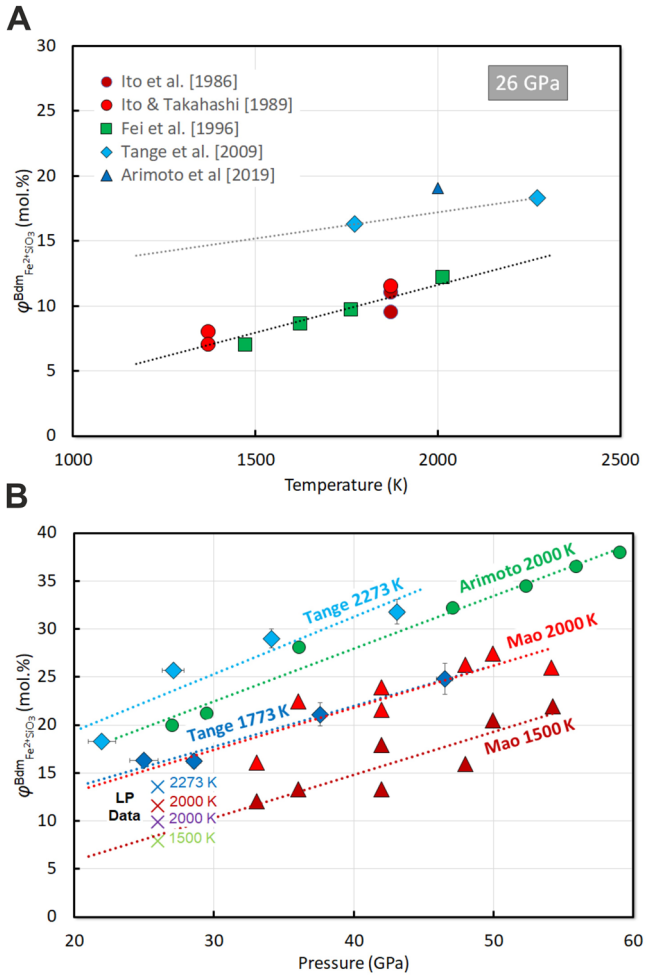

Fig. 5 | The maximum $Fe^{2+}SiO_3$ content in Bdm, $\varphi^{Bdm}_{Fe^{2+}SiO_3}$. **A** With T at *ca.* 26 GPa. Thick red circles: Ito and Takahashi[43]; red circles: Ito et al.[74]; green square: Fei et al.[75], cyan diamond: Tange et al.[76], blue triangle: Arimoto et al.[77]. **B** With P at various T. Triangles: Mao et al.[78]; Diamond: Tange et al.[76]; Circles: Arimoto et al.[77]. The crosses are the average values of Ito et al.[74], Ito and Takahashi[43], and Fei et al.[75] at *ca.* 26 GPa.

Table 2 | Thermodynamic parameters to obtain $K_{Fe^{2+}-Mg,Bdm-Fper}$ at 25 GPa

Paremter	Value
$\Delta H^0 + P\Delta V^0$	27.2 ± 6.6 KJ mol^{-1}[a]
ΔS^0	−4.0 ± 1.9 J mol^{-1} K^{-1}[a]
$W^{Bdm}_{Fe^{2+}SiO_3-MgSiO_3}$	−4.9 ± 7.6 KJ mol^{-1}[a]
$W^{Fper}_{Fe^{2+}O-MgO}$	13.2(3) KJ mol^{-1}[b]

[a]Nakajima et al.[85], [b]Frost et al.[28].

Fe^{2+}-Mg exchange coefficient with ferropericlase. The Fe-Mg exchange between Bdm and Fper is geophysically important, as Fper is the only ferromagnesian mineral coexisting with Bdm in Earth's mantle. The substitution of Mg by Fe^{2+} notably affects the physical properties of these minerals, altering their density and electrical conductivity[6,80]. The exchange coefficient of Fe^{2+} and Mg of Bdm with Fper, $K^{Bdm-Fper}_{Fe^{2+}-Mg}$, is defined as:

$$K^{Bdm-Fper}_{Fe^{2+}-Mg} = \frac{\left(\chi^{Bdm}_{Fe^{2+}SiO_3}/\chi^{Bdm}_{MgSiO_3}\right)}{\left(\chi^{Fper}_{Fe^{2+}SiO_3}/\chi^{Fper}_{MgSiO_3}\right)} \quad (1)$$

where χ^{α}_i is the fraction of the component i in phase α. While the apparent Fe-Mg exchange coefficient is significantly altered by Al incorporation[81], making direct application to Earth's mantle challenging, $K^{Bdm-Fper}_{Fe^{2+}-Mg}$ in the MgO-Fe^{2+}O-SiO_2 system remains important as a foundatioin for understanding Fe distribution in these minerals.

Numerous studies have attempted to determine $K^{Bdm-Fper}_{Fe^{2+}-Mg}$ at 23–25 GPa using MAP[43,74,83–85]. However, achieving equilibrium has been challenging. Many workers used olivine as a starting material, but this approach led to issues with low-T compositions persisting due to slow kinetics[82] and Fe^{2+} oxidation to Fe^{3+} during the dissociation[84].

Nakajima et al.[85] provided the best understanding of $K^{Bdm-Fper}_{Fe^{2+}-Mg}$ for the topmost lower mantle conditions. They measured compositions of Bdm and Fper coexisting with metallic iron at significantly high T (2400–2600 K) using various bulk compositions. This approach minimised Fe^{3+} content and allowed for chemical equilibrium and grain growth suitable for microprobe analysis. While data from Katsura and Ito[82] and Frost and Langenhorst[84] generally align with Nakajima et al.'s[85] findings, Katsura and Ito's[82] $K^{Bdm-Fper}_{Fe^{2+}-Mg}$ was higher, especially for low-Fe samples. This discrepancy may be due to significant Fe^{3+} in Bdm's B-site, caused by oxidation from B_2O_3 flux. The consistency improves for higher Fe samples because the B site's Fe^{3+} capacity is limited, reducing its impact on $K^{Bdm-Fper}_{Fe^{2+}-Mg}$.

The Fe^{2+}-Mg exchange coefficient is directly related to the chemical potential change of the Fe^{2+}-Mg exchange reaction between Bdm and Fper. This reaction can be expressed as:

$$\underset{Bdm}{MgSiO_3} + \underset{Fper}{Fe^{2+}O} = \underset{Bdm}{Fe^{2+}SiO_3} + \underset{Fper}{MgO} \quad (2)$$

The conditions for equilibrium of Eq. (1) can be written as:

$$RT\ln K^{Bdm-Fper}_{Fe^{2+}-Mg} = -\left(\Delta H^0 + P\Delta V^0 - T\Delta S^0\right) - RT\ln\frac{\left(\gamma^{Bdm}_{Fe^{2+}SiO_3}/\gamma^{Bdm}_{MgSiO_3}\right)}{\left(\gamma^{Fper}_{Fe^{2+}SiO_3}/\gamma^{Fper}_{MgSiO_3}\right)} \quad (3)$$

where ΔH^0, ΔV^0, and ΔS^0, respectively, are the enthalpy, volume, and entropy changes associated with the exchange reaction in the standard state, γ^{α}_i is the activity coefficient of the component i in phase α, R is the gas constant, and T is the absolute temperature. Using the regular solution model, the term of the acitivty coefficient can be expressed as:

$$-RT\ln\frac{\left(\gamma^{Bdm}_{Fe^{2+}SiO_3}/\gamma^{Bdm}_{MgSiO_3}\right)}{\left(\gamma^{Fper}_{Fe^{2+}SiO_3}/\gamma^{Fper}_{MgSiO_3}\right)} = W^{Bdm}_{Fe^{2+}SiO_3-MgSiO_3}\left(1-2\chi^{Bdm}_{Fe^{2+}SiO_3}\right) - W^{Fper}_{Fe^{2+}O-MgO}\left(1-2\chi^{Fper}_{Fe^{2+}O}\right) \quad (4)$$

where $W^{Bdm}_{Fe^{2+}SiO_3-MgSiO_3}$ and $W^{Fper}_{Fe^{2+}O-MgO}$, respectively, are the symmetric interaction parameters (Margules parameters) for Bdm and Fper. The parameters for this model, as determined by Nakajima et al.[85], are given in Table 2.

Figure 6A shows $K^{Bdm-Fper}_{Fe^{2+}-Mg}$ for various $\chi^{Bdm}_{Fe^{2+}SiO_3}$ as a function of T at 25 GPa calculated using the above thermodynamic parameters. The graph also includes experimental data by Katsura and Ito[82], Frost and Langenhorst[84], and Nakajima et al.[85]. As expected, $K^{Bdm-Fper}_{Fe^{2+}-Mg}$ increases with increasing T. For instance, at $\chi^{Bdm}_{Fe^{2+}SiO_3}$ of 8 mol.%, $K^{Bdm-Fper}_{Fe^{2+}-Mg}$ is 0.19 at 1800 K, whereas it is 0.30 at 2600 K. More notably, $K^{Bdm-Fper}_{Fe^{2+}-Mg}$ is strongly compositional dependent, decreasing with increasing $Fe^{2+}/(Fe^{2+} + Mg)$ ratio in the system. For instance, at 2000 K, $K^{Bdm-Fper}_{Fe^{2+}-Mg}$ is 0.32 at $\chi^{Bdm}_{Fe^{2+}SiO_3}$ of 4 mol.%. but drops to 0.16 at 16 mol.%. This compositional effect is significantly larger than the T effect, primarily due to the large $W^{Fper}_{Fe^{2+}O-MgO}$, because $W^{Bdm}_{Fe^{2+}SiO_3-MgSiO_3}$ can be assumed to be zero[85].

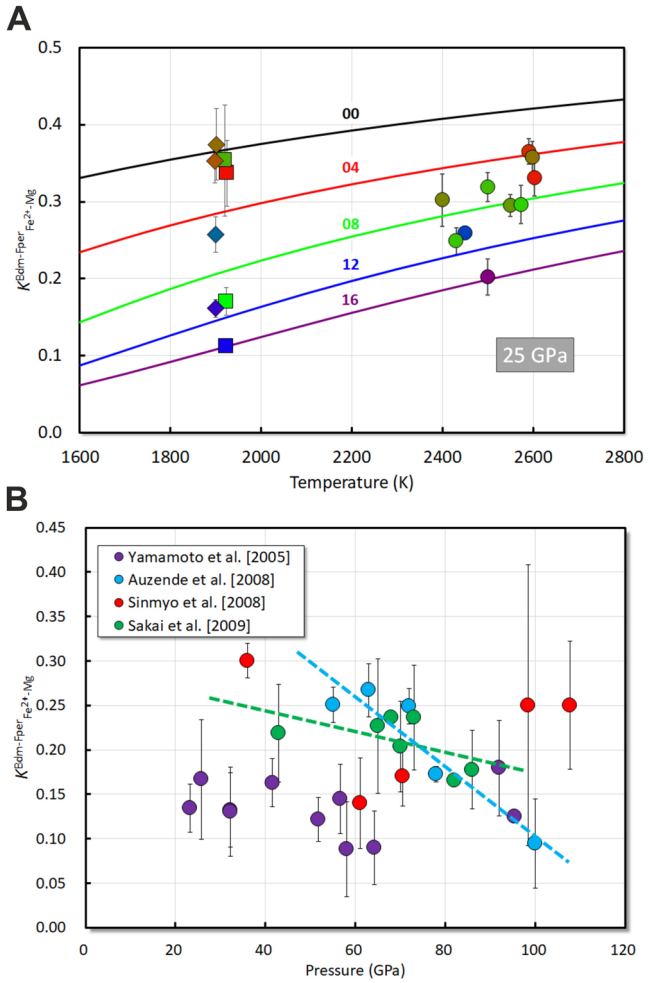

Fig. 6 | Fe^{2+}-Mg exchange coefficient between Bdm and Fper, $K_{Fe^{2+}-Mg}^{Bdm-Fper}$. **A** With *T* at 25 GPa. The symbols denote the experimental data. Circles: Nakajima et al.[85], square: Frost and Langenhorst[84], diamond: Katsura and Ito[82]. The curves are $K_{Fe^{2+}-Mg}^{Bdm-Fper}$ of $\chi_{Fe^{2+}SiO_3}^{Bdm}$ calculated using the thermodynamic parameters given by Nakajima et al.[85]. The numbers denote $\chi_{Fe^{2+}SiO_3}^{Bdm}$ in mol.%. The colors indicate $\chi_{Fe^{2+}SiO_3}^{Bdm}$: red: 4 mol.%, green: 8 mol.%, blue: 12 mol.%, and violet: 16 mol.%. The colours of the symbols also denote $\chi_{Fe^{2+}SiO_3}^{Bdm}$. **B** With *P* at relatively similar *T* and bulk compositions. Violet: 1500–1600 K using San Carlos olivine by Kobayashi et al.[9], cyan: 2000-2450 K using San Carlos olivine by Auzende et al.[88], 1800–2200 K using $(Mg_{0.89}Fe_{0.11})_2SiO_4$ gel by Sinmyo et al.[89], green: 1900–2100 K using San Carlos olivine by Sakai et al.[10]. The cyan and green broken lines showing a negative *P* dependence are fitting to the data given by Auzende et al.[88] and Sakai et al.[10].

$K_{Fe^{2+}-Mg}^{Bdm-Fper}$ has been studied at higher *P* using LH-DAC[9,78,82,86–89]. Additionally, $K_{Fe^{2+}-Mg}^{Bdm-Fper}$ can also be derived from data determining $\varphi_{Fe^{2+}SiO_3}^{Bdm}$ [8,76–78] with *P*. However, understanding the *P* dependence of $K_{Fe^{2+}-Mg}^{Bdm-Fper}$ is challenging due to its complex relationship with *T* and compositions. Figure 6A shows $K_{Fe^{2+}-Mg}^{Bdm-Fper}$ from four studies with minimal variations in *T* and bulk compositions[9,82,88,89]. Two of the studies, Auzende et al.[88] and Sakai et al.[82], showed a negative *P* dependence of $K_{Fe^{2+}-Mg}^{Bdm-Fper}$, which they attributed to the spin transition of Fper. However, Nakajima et al.[85] suggested that this *P* dependence could be interpreted without the spin transition. Given these conflicting interpretations, a comprehensive study is required to determine $K_{Fe^{2+}-Mg}^{Bdm-Fper}$ as a function of *P*, *T*, f_{O_2}, and composition precisely.

MgO-CaO-SiO$_2$. Calcium is the sixth most abundant element in Earth's mantle[1]. In the lower mantle, CaO forms Dvm[34]. Bdm and Dvm are the two main phases in the MgO-CaO-SiO_2 system. Since non-stoichiometry is not Known in Dvm, the coexistence of Sti, Per, or other Ca-bearing phases should not affect the phase relations between Bdm and Dvm. Consequently, the binary $MgSiO_3$-$CaSiO_3$ system is crucial for understanding the ternary MgO-CaO-SiO_2 system. As Bdm and Dvm melt congruently[90], the eutectic melting *T* limits the stability of Bdm at high *T* in this system. Furthermore, no phase transition of Dvm is known within Bdm's stability field at mantle temperatures.

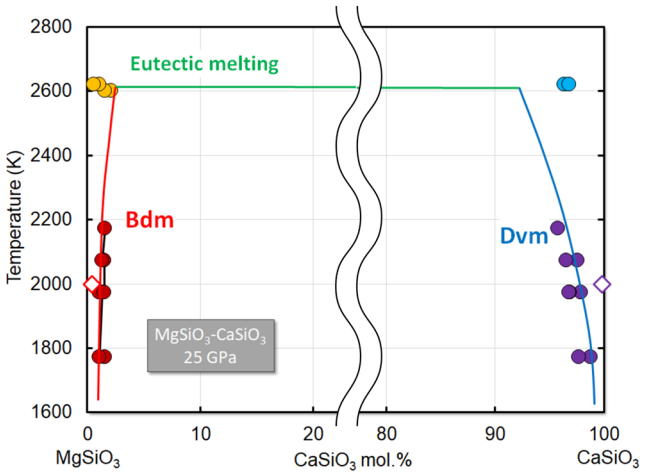

Fig. 7 | Phase relations in $MgSiO_3$-$CaSiO_3$, *i.e.*, $\varphi_{CaSiO_3}^{Bdm}$ and $\varphi_{MgSiO_3}^{Dvm}$, with *T* at 25 GPa[90,92,93,115]. The red and violet circles indicate *T* and $\varphi_{CaSiO_3}^{Bdm}$ of coexisting Bdm and Dvm, respectively, taken from Irifune et al.[92] and Irifune et al.[93]. The yellow and cyan circles, respectively, indicate *T* and $\varphi_{CaSiO_3}^{Bdm}$ of Bdm and Dvm coexisting with eutectic melt, from Nomura et al.[90]. The open red and violet diamonds indicate *T* and $\varphi_{CaSiO_3}^{Bdm}$ of coexisting Bdm and Dvm, respectively, from Nomura et al.[90].

The maximum $CaSiO_3$ content in Bdm, $\varphi_{CaSiO_3}^{Bdm}$, below the eutectic point is geochemically significant due to Ca's large ionic radius. This property allows Dvm to incorporate much larger amounts of trace elements, such as REE, U, and Th, than Bdm[91]. Consequently, the presence of Dvm significantly impacts trace element profiles in the mantle. Given that $CaSiO_3$ is relatively small compared to $MgSiO_3$ in Earth's mantle, it is crucial to determine whether $\varphi_{CaSiO_3}^{Bdm}$ exceeds the mantle's $CaSiO_3$ content. If $\varphi_{CaSiO_3}^{Bdm}$ surpasses 8 mol.%, it would imply that all Ca is contained in Bdm, and Dvm does not exist in the lower mantle. This determination is essential for understanding the distribution of calcium and associated trace elements in the lower mantle.

The phase relations of Bdm and Dvm in the $MgSiO_3$-$CaSiO_3$ system under topmost lower-mantle conditions (24 GPa) have been studied using MAP[90,92,93]. Eutectic melting occurs between 2620 and 2700 K at this *P* [90] (Fig. 7). $\varphi_{CaSiO_3}^{Bdm}$ is very low, limited to 2 mol.% even at the eutectic *T*, suggesting Dvm's presence in the top of the lower mantle.

It remains unknown whether $\varphi_{CaSiO_3}^{Bdm}$ reaches 8 mol.% at higher *P*. As the eutectic *T* should increase with pressure, the maximum *T* of Bdm stability may increase, potentially resulting in higher $\varphi_{CaSiO_3}^{Bdm}$. The miscibility gap between Bdm and Dvm could narrow with increasing *P* if the partial molar volume of $CaSiO_3$ in Bdm is smaller than Dvm's molar volume. In situ X-ray studies with MAP observed metastable Ca-rich Bdm formation at various *P* and *T*, but it transformed to Bdm + Dvm at higher *T* [19,93]. The volumes of Ca-rich Bdm were reported to be larger than Bdm + Dvm[19], suggesting the miscibility gap is unlikely to narrow with increasing *P*. Recent laser-heated diamond anvil cells (LH-DAC) studies reported the formation of Ca-rich Bdm at high *P* and *T* in Fe- and Al-bearing systems[11,94]. Reference 12 suggested that the secondary components of Fe and Al promoted $\varphi_{CaSiO_3}^{Bdm}$. It is noted that, however, Raoult's law implies that the presence of minor components does not significantly alter the thermodynamic properties of the major component. Further investigation is necessary to reach conclusive results about $\varphi_{CaSiO_3}^{Bdm}$ at higher *P*.

MgO-Al_2O_3-SiO_2. Al is the sixth most abundant element in the Earth's mantle[1]. Significant quantities of Al_2O_3 can be present in Bdm, depending on prevailing conditions. Extensive research has been conducted on the phase relations in the MgO-Al_2O_3-SiO_2 system[16,22,23,95–110]. Figure 8A illustrates the phase assemblage in this system at 27 GPa and 2000 K[38]. As the Mg/Si ratio decreases from infinite to zero, the phases coexisting with Bdm change from Per, Per + PS[111,112], PS, PS + corundum (Crn), Crn, Crn + Sti, and Sti. This PS has a $CaFe_2O_4$-structure[111], with $MgAl_2O_4$ as its primary component, but can contain Mg_2SiO_4[113]. Similarly, Crn's primary component is Al_2O_3, but it can contain $MgSiO_3$[37,98,100,114]. At these conditions, the Mg_2SiO_4 and $MgSiO_3$ contents in $CaFe_2O_4$-type PS and Crn coexisting with Bdm are 29-34 and 19-21 mol.%, respectively[38]. The Al_2O_3 contents in Per and Sti coexisting with Bdm are limited to 0.5 and 5 mol.%, respectively. Notably, the Al_2O_3 content in Sti may be attributed to H_2O potential incorporation through the substitution $Si^{4+} \leftrightarrow Al^{3+} + H^{+}$ [42].

Al is primarily incorporated into Bdm as CC, Al_2O_3, especially when the Mg/Si ratio is unity, where the coexisting phase is Crn[22,37,98,100,102,106,114,115].

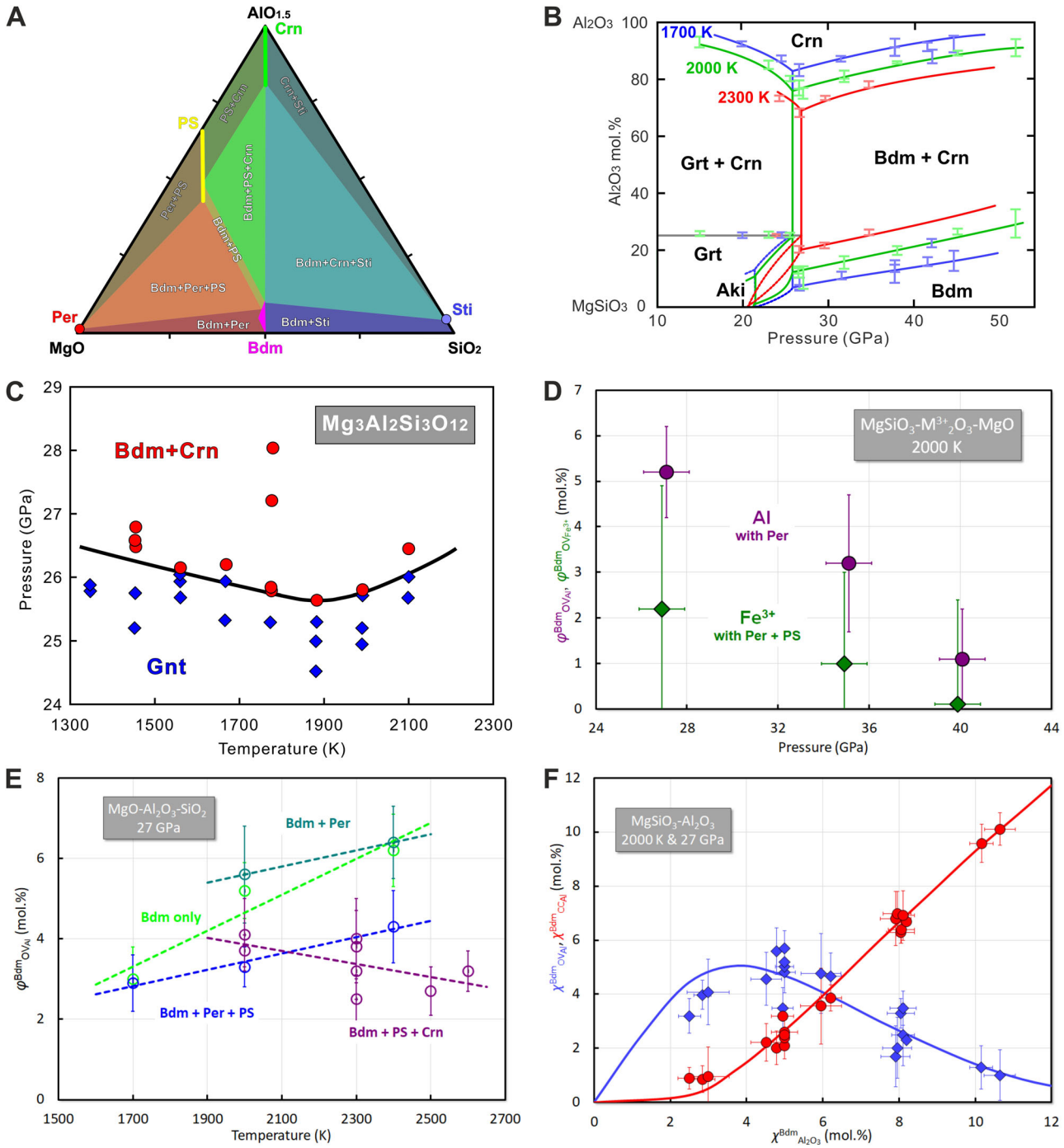

Fig. 8 | Bdm's phase relations in MgO-Al2O3-SiO2. A Phase assemblage at 27 GPa and 2000 K. Modified from Liu et al.[37]. **B** Phase relations in $MgSiO_3$-Al_2O_3 at 1700, 2000, and 2300 K and up to 50 GPa. The phase relations of Bdm, Gnt, and Aki were only studied near 2000 K. Modified from Liu et al.[37,114]. **C** Gnt to Bdm + Crn transition. Modified from Ishii et al.[16]. **D** $\varphi^{Bdm}_{MgAlO_{2.5}}$ and $\varphi^{Bdm}_{MgFe^{3+}O_{2.5}}$ in Bdm with *P* at 2000 K. Based on Liu et al.[110] and Fei et al.[123]. **E** $\varphi^{Bdm}_{OV_{Al}}$ with *T* at 27 GPa. Violet: coexisting with PS and Crn, blue: coexisting with Per and PS, blue-green: coexisting with Per, light green: no coexisting phase. The coloured broken lines indicate the *T* dependence of $\varphi^{Bdm}_{OV_{Al}}$ with various coexisting phases. **F** $\chi^{Bdm}_{OV_{Al}}$ and $\chi^{Bdm}_{CC_{Al}}$ coexisting with Per with $\chi^{Bdm}_{Al_2O_3}$ at 2000 K and 27 GPa. Modified from Huang et al.[81].

Table 3 | Thermodynamic parameters to describe Bdm and Fper chemistry in MgO-Al_2O_3-SiO_2 at 27 GPa and 2000 K from Huang et al.[81]

Parameter	Value
$W^{Bdm}_{Al-Si,B}$	−30(2) KJ mol^{-1}
$W^{Bdm}_{Mg-Al,A}$	0
$W^{Bdm}_{O-\square,O1}$	0
$\Delta G_{(5)}{}^{0}$	−19.5(15) KJ mol^{-1}

The maximum Al_2O_3 CC content in Bdm, $\varphi^{Bdm}_{CC_{Al}}$, increases with P [37,98,100,102,114,115] (Fig. 8B). For example, $\varphi^{Bdm}_{CC_{Al}}$ increases from 12 to 22 mol.% as P rises from 27 to 42 GPa at 2000 K[114]. Notably, when the $\varphi^{Bdm}_{CC_{Al}}$ is high (at least 25 mol.%), Bdm cannot be recovered to ambient conditions but transforms to the $LiNbO_3$ structure upon decompression[109,114]. The increase in $\varphi^{Bdm}_{CC_{Al}}$ with P is associated with a decrease in the maximum $MgSiO_3$ content in Crn, $\varphi^{Crn}_{MgSiO_3}$. For instance, $\varphi^{Crn}_{MgSiO_3}$ decreases from 32 to 22 mol.% as P rises from 27 to 35 GPa at 2300 K. Similarly, $\varphi^{Bdm}_{CC_{Al}}$ increases with T [22,37,114]. For instance, $\varphi^{Bdm}_{CC_{Al}}$ increases from 16 to 30 mol.% as T rises from 1700 to 3000 K at 27 GPa. This increase is accompanied by a corresponding increase in $\varphi^{Crn}_{MgSiO_3}$.

The stability field of Bdm + Crn in the $MgSiO_3$-Al_2O_3 system is constrained on the lower P side by the formation of pyrope Gnt[16,98,100,101] at 26 GPa (Fig. 8C). The boundary in the P-T space is curved. The dP/dT is negative, with a value of −1.5 MPaK^{-1} at 1400–1800 K. At higher T up to 1900–2100 K, dP/dT becomes positive, reaching a value of +2.5 MPaK^{-1}. At high P, *ca.* 100 GPa, Crn first transforms to the Rh_2O_3(II) structure[116]. The melting relations in the Bdm + Crn system have not yet been investigated.

In MgO-rich or SiO_2-poor systems, Bdm contains OV, $MgAlO_{2.5}$, in addition to CC[103,107,110,117–119]. The maximum OV content, $\varphi^{Bdm}_{OV_{Al}}$, is considerably more limited than $\varphi^{Bdm}_{CC_{Al}}$ [103,110,118,119]. $\varphi^{Bdm}_{OV_{Al}}$ rapidly decreases with P[110], as shown in Fig. 8D. For instance, $\varphi^{Bdm}_{OV_{Al}}$ decreases from 6 to 1 mol.% as P rises from 27 to 40 GPa at 2000 K when coexisting with Per. The T dependence of $\varphi^{Bdm}_{OV_{Al}}$ varies based on the coexisting phases (Fig. 8E)[119]. When Bdm coexists with Per and Per + PS, respectively, $\varphi^{Bdm}_{OV_{Al}}$ increases from 3 to 6 mol.% and from 3 to 4 mol.%, respectively, as T rises from 1700 to 2300 K. However, when coexisting with PS + Crn, $\varphi^{Bdm}_{OV_{Al}}$ decreases from 4 to 3 mol.% as T rises from 2000 to 2300 K[23]. Generally, the T dependence of $\varphi^{Bdm}_{OV_{Al}}$ decreases with increasing the Al_2O_3 content, *i.e.*, in the order of Per → Per + PS → PS + Crn.

The local chemical environment of Al^{3+} in OV is complex. Nuclear magnetic resonance (NMR) studies have indicated that Al^{3+} in Bdm can have coordination numbers of 4, 5, 6, and 8[29,120,121]. Among these, 6-coordinated Al^{3+} are predominant, suggesting a random distribution of Al^{3+} and O^{2-} vacancies. However, the presence of 4-coordinated Al^{3+} indicates the formation of clusters comprising both Al^{3+} and O^{2-} vacancies.

The variation in the OV content, $\varphi^{Bdm}_{OV_{Al}}$, is more complex than $\varphi^{Bdm}_{CC_{Al}}$. When the bulk Al_2O_3 content in Bdm, $\chi^{Bdm}_{Al_2O_3} = \chi^{Bdm}_{CC_{Al}} + 0.5\chi^{Bdm}_{OV_{Al}}$, increases to approximately 10 mol.% in the presence of Per, the $\chi^{Bdm}_{OV_{Al}}$ initially increases and then decreases at $\chi^{Bdm}_{Al_2O_3}$. In contrast, $\chi^{Bdm}_{CC_{Al}}$ increases monotonically (Fig. 8F).

Huang et al.[81] employed a thermodynamic approach to express the equilibrium of Bdm and Per in the MgO-Al_2O_3-SiO_2 system. To address the complexity of OV, they introduced the $MgSi_{\frac{7}{8}}Al_{\frac{1}{8}}O_{\frac{15}{16}\frac{1}{16}}O_2$ component instead of $MgAlO_{2.5}$. This equilibrium was represented by the following equation:

$$\underset{Brg}{MgSi_{\frac{7}{8}}Al_{\frac{1}{8}}O_{\frac{15}{16}}\square_{\frac{1}{16}}O_2} = \frac{1}{16}\underset{Brg}{AlAlO_3} + \frac{7}{8}\underset{Brg}{MgSiO_3} + \frac{1}{8}\underset{Per}{MgO} \quad (5)$$

The standard Gibbs energy of reaction (5) at equilibrium, $\Delta G_{(5)}{}^{0}$, was expressed using the following equation:

$$\Delta G^0_{(5)} = -RT\ln\frac{\left(a^{Bdm}_{AlAlO_3}\right)^{\frac{1}{16}}\left(a^{Bdm}_{MgSiO_3}\right)^{\frac{7}{8}}\left(a^{Per}_{MgO}\right)^{\frac{1}{8}}}{a^{Bdm}_{MgSi_{\frac{7}{8}}Al_{\frac{1}{8}}O_{\frac{15}{16}}\square_{\frac{1}{16}}O_2}} \quad (6)$$

where a^{A}_{i} is the activity of component i in phase A. To consider the fraction of $MgSi_{\frac{7}{8}}Al_{\frac{1}{8}}O_{\frac{15}{16}}\square_{\frac{1}{16}}O_2$, $\chi^{Bdm}_{MgSi_{\frac{7}{8}}Al_{\frac{1}{8}}O_{\frac{15}{16}\frac{1}{16}}O_2}$, they assumed that O^{2-} vacancies occur on the O1 site (multiplicity of unity) and not on the O2 site (multiplicity of two). This results in:

$$\chi^{Bdm}_{MgSi_{\frac{7}{8}}Al_{\frac{1}{8}}O_{\frac{15}{16}}\square_{\frac{1}{16}}O_2} = 1.841x^{Bdm}_{Mg_A}\left(x^{Bdm}_{Al_B}\right)^{\frac{1}{8}}\left(x^{Bdm}_{Si_B}\right)^{\frac{7}{8}}\left(x^{Bdm}_{\square_{O1}}\right)^{\frac{1}{16}}\left(x^{Bdm}_{O_{O1}}\right)^{\frac{15}{16}} \quad (7)$$

where $x^{Bdm}_{Mg_A}$, $x^{Bdm}_{Al_B}$, and $x^{Bdm}_{Si_B}$ are the fractions of Mg on the A site, Al and Si on the B site, respectively, and x^{Bdm}_{O1} and $x^{Bdm}_{O_{O1}}$ are the fractions of vacancies and oxygen on the O1 site, respectively. The coefficient 1.841 ensures that the activity of the endmember $MgSi_{7/8}Al_{1/8}O_{15/16}\square_{1/16}O_2$ equals unity and is driven from $1/\left(\frac{1}{8}\right)^{\frac{1}{8}}\left(\frac{7}{8}\right)^{\frac{7}{8}}\left(\frac{1}{16}\right)^{\frac{1}{16}}\left(\frac{15}{16}\right)^{\frac{15}{16}}$.

The $MgSiO_3$ fraction in Bdm, $\chi^{Bdm}_{MgSiO_3}$, was expressed as follows:

$$\chi^{Bdm}_{MgSiO_3} = x^{Bdm}_{Mg,A}x^{Bdm}_{Si,B}x^{Bdm}_{O,O1} \quad (8)$$

The regular symmetric solution model was used to express the activity coefficient of $MgSi_{7/8}Al_{1/8}O_{15/16}\square_{1/16}O_2$, $\gamma^{Bdm}_{MgSi_{\frac{7}{8}}Al_{\frac{1}{8}}O_{\frac{15}{16}}\square_{\frac{1}{16}}O_2}$:

$$RT\ln\gamma^{Bdm}_{MgSi_{\frac{7}{8}}Al_{\frac{1}{8}}O_{\frac{15}{16}}\square_{\frac{1}{16}}O_2} = W^{Bdm}_{Mg-Al,A}\left(1-x^{Bdm}_{Mg,A}\right)^2 + W_{Al-Si,B}\left(1-x^{Bdm}_{Al,B}\right)^2 + W^{Bdm}_{O-\square,O1}\left(1-x^{Bdm}_{\square,O1}\right)^2 \quad (9)$$

where $W^{Bdm}_{i\text{-}j,\alpha}$ are the interaction parameters between components i and j in the α site in Bdm. Similar expressions were provided for the activity coefficients of $MgSiO_3$ and $AlAlO_3$:

$$RT\ln\gamma^{Bdm}_{MgSiO_3} = W^{Bdm}_{Al-Si,B}\left(1-x^{Bdm}_{Si,B}\right)^2 \quad (10)$$

$$RT\ln\gamma^{Bdm}_{Al_2O_3} = W^{Bdm}_{Al-Si,B}\left(1-x^{Bdm}_{Al_B}\right)^2 \quad (11)$$

The parameters evaluated by Huang et al.[81] are presented in Table 3. This formulation and the estimated parameters provide a comprehensive description of $\chi^{Bdm}_{OV_{Al}}$ and $\chi^{Bdm}_{CC_{Al}}$ in relation to $\chi^{Bdm}_{Al_2O_3m}$, as illustrated in Fig. 8F.

MgO-$Fe^{3+}{}_2O_3$-SiO_2. Despite Fe being the fourth most abundant element in Earth's mantle[1], Fe^{3+} was previously thought to play a minor role in the lower mantle. This assumption was based on the presumed reducing conditions of the lower mantle, inferred from its contact with the outer core. As a result, phase relations in the MgO-$Fe^{3+}{}_2O_3$-SiO_2 system have not been extensively studied. Another factor contributing to the limited study on this system is the difficulty in maintaining and accurately measuring Fe valence during and after high P-T experiments, making it challenging to obtain reliable data on Fe^{3+} behaviour under lower-mantle conditions.

The phase relations in the MgO-$Fe^{3+}{}_2O_3$-SiO_2 system are similar to those in the MgO-Al_2O_3-SiO_2 system[20,30,122,123]. Fe^{3+} can occupy the A- and B-sites, like Al^{3+}. However, the coexisting phases with Bdm have not been precisely determined as a function of the Mg/Fe^{3+}/Si ratio. As the Mg/Fe^{3+} ratio decreases at Mg/Si ratios less than 1:1, the coexisting phases change from Per, Per + PS, and PS,[20,122,123] (Fig. 9). This PS has a $MgFe_2O_4$

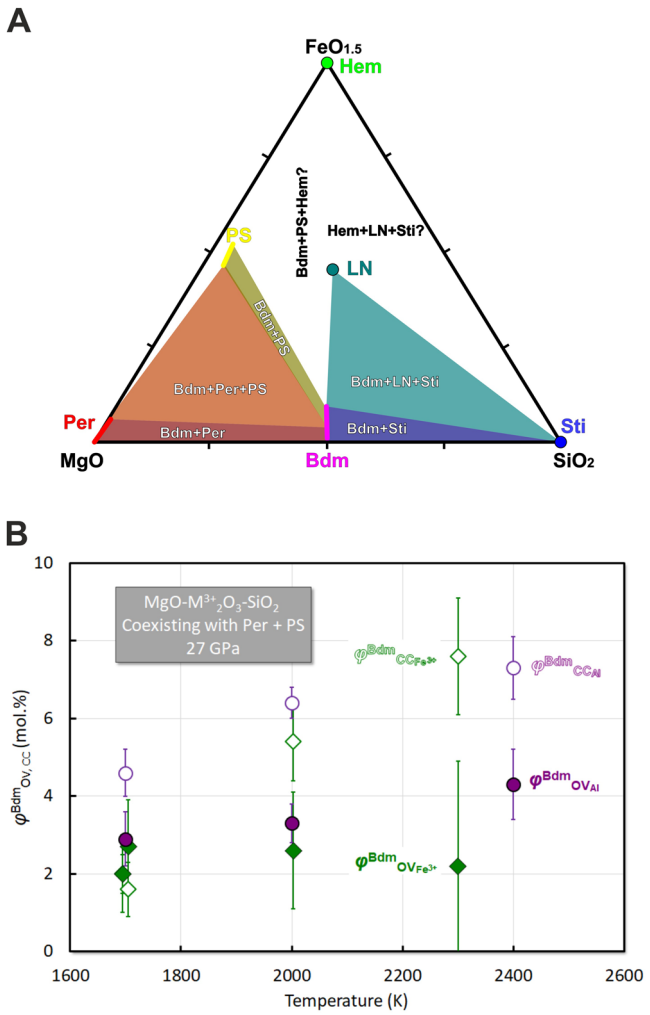

Fig. 9 | Phase relations in MgO-$Fe^{3+}{}_2O_3$-SiO_2. **A** Ternary diagram at 27 GPa and 2000~2300 K. **B** $\varphi^{Bdm}_{CC,OV}$ for Fe^{3+} and Al coexisting with Per and PS with *T* at 27 GPa. Green: Fe^{3+}; Violet: Al; Closed symbols: OV; Open symbols: CC.

composition and a $CaMn_2O_4$ structure. At Mg/Si ratios greater than 1:1, Bdm coexists with Sti and an unidentified phase with a $LiNbO_3$ structure after recovery[30]. This phase has a composition of approximately Mg/Si = 1:1 and $MgSiO_3/Fe_2O_3$ = 1:2 at 27 GPa and 1700 to 2000 K. It is possible that this $LiNbO_3$-structured phase may also have a perovskite structure at high pressure, suggesting a potential miscibility gap in perovskite phases within the $MgSiO_3$-Fe_2O_3 system. At Mg/Si ≈ 1, Bdm or the $LiNbO_3$-structured phase should coexist with a Fe_2O_3 polymorph. Although numerous Fe_2O_3 polymorphs exist[124], it is unclear which one coexists with Bdm under specific *P*-*T* conditions. Bykova et al.[124] proposed a series of phase transitions for Fe_2O_3 with *P*: α-phase (hematite, Hem) → ι-phase (Rh_2O_3(II) structure) at 25-45 GPa → ζphase (distorted perovskite structure) at 45-55 GPa → η-phase ($CaIrO_3$ structure).

The incorporation of Fe^{3+} is more limited than that of Al^{3+}. While the maximum Fe^{3+} CC content in Bdm, $\varphi^{Bdm}_{CC_{Fe^{3+}}}$, coexisting with Fe_2O_3 phases has not been studied, research on $\varphi^{Bdm}_{CC_{Fe^{3+}}}$ in other systems suggests its comparable significance at top lower mantle *P*. For instance, $\varphi^{Bdm}_{CC_{Fe^{3+}}}$ increases from 2 to 8 mol.% as *T* rises from 1700 to 2300 K when coexisting with Per and PS at 27 GPa[20], which is a similar increases in $\varphi^{Bdm}_{CC_{Al}}$ from 4 to 7 mol.% under the same conditions[119] (Fig. 9B).

P appears to have contrasting effects on $\varphi^{Bdm}_{CC_{Fe^{3+}}}$ and $\varphi^{Bdm}_{CC_{Al}}$. As *P* rises from 27 to 40 GPa at 2300 K, $\varphi^{Bdm}_{CC_{Fe^{3+}}}$ decreases from 8 to 5 mol.% when coexisting with Per and PS[123]. Conversely, $\varphi^{Bdm}_{CC_{Al}}$ increases from 12 to 22 mol.% as *P* increases from 27 to 42 GPa at 2000 K when coexisting with Crn[114]. It should be noted, however, that these two data sets cannot be directly compared due to the difference in the coexisting phase.

Unlike Fe^{3+} CC, the Fe^{3+} OV component, $MgFe^{3+}O_{2.5}\square_{0.5}$, is more limited compared to its Al counterpart, $MgAlO_{2.5}\square_{0.5}$. When coexisting with Per and PS, $\varphi^{Bdm}_{OV_{Fe^{3+}}}$ remains around 2 mol.% between 1700 and 2300 K at 27 GPa[20] (Fig. 9B). Contrastly, $\varphi^{Bdm}_{OV_{Al}}$ increases from 3 to 4 mol.% under similar conditions[119]. The formation of both Fe^{3+} and Al OV is inhibited by *P*, which is more profound for Fe^{3+}. As *P* rises from 27 to 40 GPa at 2300 K, $\varphi^{Bdm}_{OV_{Fe^{3+}}}$ decreases from 3 to 0 mol.%, showing a more significant reduction compared to $\varphi^{Bdm}_{OV_{Al}}$ (Fig. 8D).

Huang et al.[81] extended their thermodynamic approach from the Mg-Al-Si-O system to investigate the phase equilibrium of Bdm coexisting with Fper in the Mg-Fe^{3+}-Si-O system. They proposed a reaction similar to Eq. (5):

$$\underset{Bdm}{MgSi_{\frac{7}{8}}Fe^{3+}_{\frac{1}{8}}O_{\frac{15}{16}}\square_{\frac{1}{16}}O_2} = \frac{1}{16}\underset{Bdm}{Fe^{3+}Fe^{3+}O_3} + \frac{7}{8}\underset{Bdm}{MgSiO_3} + \frac{1}{8}\underset{Per}{MgO} \quad (12)$$

Thermodynamic parameters for this model were suggested (as listed in Table 4). However, the model's accuracy in reproducing experimental data is unsatisfactory. This imprecision likely stems from the limited number of experiments conducted on this system and the potential for Fe^{3+} to be reduced to Fe^{2+} during experiments.

Table 4 | Thermodynamic parameters to describe Bdm and Fper chemistry in MgO-Fe^{3+}-SiO_2 at 27 GPa and 2000 K

Parameter	Value
$W^{Bdm}_{Fe^{3+}-Si,B}$	−28(2) KJmol^{-1}
$W^{Bdm}_{Mg-Fe^{3+},A}$	11
$W^{Bdm}_{O-\square,O1}$	0
$\Delta G^{0}_{(12)}$	−21 KJ mol^{-1}

From Huang et al.[81]

MgO-$FeAlO_3$-SiO_2. Due to the similarity in ionic radii between Fe^{3+} and Al and between Mg and Si, it is expected that the Fe^{3+} and Al would predominantly occupy the A- and B-sites, respectively[125]. This expectation has been confirmed by single-crystal X-ray diffraction[125]. Notably, even under reduced conditions, Fe in Fe, Al-bearing Bdm remains predominantly Fe^{3+} through coupling with Al[27,71].

This coupling is thought to promote the formation of CC of $FeAlO_3$ while inhibiting OV. Consequently, the maximum CC fraction of $FeAlO_3$, $\varphi^{Bdm}_{CC_{FeAl}}$, is much larger than $\varphi^{Bdm}_{CC_{Al}}$ and $\varphi^{Bdm}_{CC_{Fe^{3+}}}$[21,126,127]. At 27 GPa and 2000 K, $\varphi^{Bdm}_{CC_{FeAl}}$ reaches 67 mol.%, when Bdm coexists with Crn and Hem. Notably, Bdm with $\chi^{Bdm}_{CC_{FeAl}}$ exceeding 40 mol.% transforms to the $LiNbO_3$ structure upon decompression[21,24], similar to Al_2O_3-rich Bdm[109,114]. When the Fe and Al contents are equal, the OV content is virtually zero[25,125]. A small quantity of $MgAlO_{2.5}\square_{0.5}$ is observed when the Al content exceeds the Fe content[125].

While the phase relations in the MgO-$FeAlO_3$-SiO_2 remain largely unexplored, those in the MgO-$FeAlO_3$-$MgSiO_3$ system were studied at 1700–2300 K at 27 GPa[25]. Under these conditions, Bdm coexisted with PS, primarily composed of $MgAl_2O_4$ and $MgFe_2O_4$ (likely with a $CaTi_2O_4$-type structure), and minor Crn. Bdm's main composition was 28–32 mol.% $MgSiO_3$, 65–68 mol.% $FeAlO_3$ with minor Fe_2O_3. The formation of Crn and the incorporation of Fe_2O_3 in Bdm suggest that Bdm favours Fe_2O_3 over Al_2O_3. Despite a slight increase in $FeAlO_3$ with rising *T*, no significant compositional changes were observed across the *T* range.

Table 5 | Parameters for calculating the Gibbs free energy of the end members of Bdm and Fper

	F_0 (kJ mol^{-1})	V_0 (cm^{3}mol^{-1})	K (GPa)	K'	Θ_0	γ_0	q_0
$MgSiO_3$ (Bdm)	−1362.443	24.45	251	4.1	880	1.54	0.84
$FeSiO_3$ (Bdm)	−1002.663	25.32	271	4.01	746	1.54	0.84
$FeFeO_3$ (Bdm)	−537(5)	29.55	157	4	444(13)	1.54	0.84
$AlAlO_3$ (Bdm)	−1517.729	24.94	242	4.1	858	1.54	0.84
$FeAlO_3$ (Bdm)	−1107(3)	26.90	220	4.1	697(8)	1.54	0.84
$MgAlO_{2.5}$ (Bdm)	−1379(5)	26.65	155	4.1	799(3)	1.54	0.84
MgO (Fper)	−569.527	11.25	161	3.9	771	1.45	1.55
$Fe^{2+}O$ (Fper)	−243.652	12.26	161	4	454	1.45	1.55

From Wang et al.[26]

Table 6 | Interaction parameters for the excess enthalpy in the solution mixing model

Parameter	Value (kJ mol^{-1})
$W^{Bdm}_{MgSiO_3-AlAlO_3}$	35
$W^{Bdm}_{MgSiO_3-Fe^{2+}SiO_3}$	−11.4
$W^{Bdm}_{MgSiO_3-MgAlO_{2.5}\square_{0.5}}$	222(2)
$W^{Fper}_{MgO-Fe^{2+}O}$	13.7

From Wang et al.[26]

MgO-FeO-Fe_2O_3-Al_2O_3-SiO_2. This system is most relevant for understanding Bdm chemistry in the lower mantle. However, its complexity, with five components, makes comprehending phase relations extremely challenging. The difficulty in directly controlling the $Fe^{3+}/\Sigma Fe$ ratio further complicates investigations. Some studies assume that the initial $Fe^{3+}/\Sigma Fe$ in starting materials remains unchanged during a high P-T experiment in LH-DAC experiments[12]. This assumption is quite questionable, especially at high T due to diffusion[13]. Indeed, measurements of $Fe^{3+}/\Sigma Fe$ in Bdm have yielded inconsistent results across various studies[12,13,128–131], suggesting that bulk $Fe^{3+}/\Sigma Fe$ likely changes during high P-T experiments.

In contrast to the conventional approach of maintaining constant bulk $Fe^{3+}/\Sigma Fe$, some studies have estimated f_{O_2} based on the equilibrium between Fe-bearing phases with different valence states in the run products[79,81]. Specifically, f_{O_2} is estimated using the reaction between Fe-bearing alloy and ferropericlase:

$$2\underset{\text{alloy}}{\text{Fe}} + O_2 = 2\underset{\text{Fper}}{\text{FeO}} \tag{13}$$

To produce an alloy, a platinum group metal, typically Ir, is added, as it is not incorporated into the silicate or oxide phase. Using reaction (13), f_{O_2} is calculated with the following equation:

$$\log f_{O_2} = \frac{2\mu^{Fper}_{Fe^{2+}O} - 2\mu^{alloy}_{Fe}}{\ln 10RT} = \frac{\Delta G^0_{P,T(13)}}{\ln 10RT} + 2\log\left(\gamma^{Fper}_{Fe^{2+}O}\chi^{Fper}_{Fe^{2+}O}\right) - 2\log\left(\gamma^{alloy}_{Fe}\chi^{alloy}_{Fe}\right) \tag{14}$$

The phase relations of Bdm and Fper in the MgO-FeO-Fe_2O_3-Al_2O_3-SiO_2 are described based on Wang et al.[26].

The two exchange coefficients are defined as follows:

$$K^{Bdm-Fper}_{Fe^{2+}-Mg} = \frac{\chi^{Bdm}_{Fe^{2+}SiO_3}}{\chi^{Bdm}_{MgSiO_3} + \chi^{Bdm}_{MgAlO_{2.5}\square_{0.5}}} \Big/ \frac{\chi^{Fper}_{Fe^{2+}O}}{\chi^{Fper}_{MgO}} \tag{15}$$

$$K^{Bdm-Fper}_{\Sigma Fe-Mg} = \frac{\chi^{Bdm}_{Fe^{2+}SiO_3} + 2\chi^{Bdm}_{Fe^{3+}Fe^{3+}O_3} + \chi^{Bdm}_{Fe^{3+}AlO_3}}{\chi^{Bdm}_{MgSiO_3} + \chi^{Bdm}_{MgAlO_{2.5}\square_{0.5}}} \Big/ \frac{\chi^{Fper}_{Fe^{2+}O}}{\chi^{Fper}_{MgO}} \tag{16}$$

Unlike the previous definition of $K^{Bdm-Fper}_{Fe^{2+}-Mg}$, Eq. (15) includes $\chi_{MgAlO_{2.5}\square_{0.5},Bdm}$ to account for all Mg. $K^{Bdm-Fper}_{\Sigma Fe-Mg}$ is referred to as the "apparent" exchange coefficient, incorporating both Fe^{2+} and Fe^{3+}[27,81,84,85]. This value is obtained by electron microprobe analysis without distinguishing Fe^{2+} and Fe^{3+}.

Wang et al.[26] described the equilibrium of Bdm and Fper in the current system using the following reactions in addition to reaction (2):

$$2\underset{\text{Bdm}}{\text{MgAl}\left[O_{0.5}\square_{0.5}\right]O_2} = \underset{\text{Bdm}}{\text{AlAl[O]O}_2} + 2\underset{\text{FPer}}{\text{MgO}} \tag{17}$$

$$2\underset{\text{FPer}}{Fe^{2+}O} + 0.5O_2 = \underset{\text{Bdm}}{Fe^{3+}Fe^{3+}O_3} \tag{18}$$

$$\underset{\text{Bdm}}{Fe^{3+}Fe^{3+}O_3} + \underset{\text{Bdm}}{AlAlO_3} = 2\underset{\text{Bdm}}{AlFe^{3+}O_3} \tag{19}$$

The thermodynamics framework, based on the work of Stixrude and Lithgow-Bertelloni[132,133], begins with the following expression for the Helmholtz energy, F, of the endmembers:

$$\begin{aligned} F(V,T_1) = {} & F(V_0,T_0) + \frac{9V_0K_{T0}}{2}f_E^2 + \frac{9V_0K_{T0}\left(K'_{T0}-4\right)}{2}f_E^3 \\ & + 9nk_B\left[T_1D\left(\frac{\theta}{T_1}\right) - T_0D\left(\frac{\theta}{T_0}\right)\right] \\ & + \left[F_{mag}(V_0,T_1) - F_{mag}(V_0,T_0)\right] \end{aligned} \tag{20}$$

where K_{T0} and K_{T0}' are the bulk modulus and its pressure derivative, f_E is the Murnaghan's finite stran[134], k_B is the Boltzmann constant, θ is the Debye temperature, D is the Debye function[135], and F_{mag} is the magnetic contribution of iron to F. Wang et al.[26] applied a symmetric regular solution model to determine Bdm and Fper compositions. The parameters provided are presented in Tables 5 and 6.

We can obtain various insights about Brm and Fper's chemistry from the above formula and parameters. To show some examples, I have simulated the various contents in Bdm and Fper and the exchange coefficients in a bulk composition similar to pyrolite by varying, f_{O_2}, T, P, Fe/Mg, and Al/Si, whose results are given in the supplementary information. The most important insight from these investigations is that Bdm $Fe^{3+}/\Sigma Fe$ is non-zero but is several-tenths even at f_{O_2} below the IW buffer (Fig. S1A). Bdm $Fe^{3+}/\Sigma Fe$ particularly increases from less than 0.1 to about 0.6 as rising Al/Si from 0 to 0.3, indicating that the Fe^{3+} content is due to the coupling of Fe^{3+} and Al, especially the high stability of $[Fe^{3+}]_A[Al^{3+}]_BO^{2-}{}_3$ (Fig. S1I).

From an Earth science perspective, this property of Bdm results in the disproportionation of Fe^{2+} into Fe^0 and Fe^{3+}[136].

$$3FeO = Fe + Fe_2O_3 \quad (21)$$

In peridotite systems, this disproportionation involves Fper:

$$3\,\underset{\text{Fper}}{Fe^{2+}O} + \underset{\text{Bdm}}{AlAlO_3} = Fe + 2\,\underset{\text{Bdm}}{AlFe^{3+}O_3} \quad (22)$$

While $Fe^{3+}/\Sigma Fe$ observed in upper-mantle rocks is only about 0.04[137], Bdm constitutes 80% of pyrolite with Bdm $Fe^{3+}/\Sigma Fe$ of several tenths at various P, T and f_{O2} (Fig. S1A, C, E). Consequently, free metallic iron is likely present in the lower mantle[136,137].

H_2O bearing systems. Many studies have been conducted to determine the maximum H_2O content in Bdm, $\varphi^{Bdm}_{H_2O}$[138–148]. As excess H_2O coexisting with silicate forms a hydrous melt under mantle conditions, the coexistence with hydrous melt is essential for determining $\varphi^{Bdm}_{H_2O}$. A challenge in determining $\varphi^{Bdm}_{H_2O}$ is the potential presence of hydrous mineral inclusions[140]. As $\varphi^{Bdm}_{H_2O}$ is typically minimal, such inclusions can lead to erroneous interpretation of $\varphi^{Bdm}_{H_2O}$.

$\varphi^{Bdm}_{H_2O}$ in $MgSiO_3$ Bdm was first reported by Meade et al.[138] as 60–70 wt. ppm, using a 200 μm single crystal synthesised by Ito and Weidner[149]. Litasov et al.[141] later reported 100 wt. ppm H_2O, but their smaller crystal size (100 μm) may have led to the broadband signals from the grain boundary rather than the crystal interior. The sharp peaks in their study indicated only 40 wt. ppm H_2O. In contrast, Bolfan-Casanova et al.[140] detected only 1 ~ 2 wt. ppm H_2O, suggesting that higher reported $\varphi^{Bdm}_{H_2O}$ might be due to inclusions. Recently, Liu et al.[145] measured $\varphi^{Bdm}_{H_2O}$ using a large (300 μm) single crystal and reported that it is less than 50 wt. ppm. Considering these studies, $\varphi^{Bdm}_{H_2O}$ in $MgSiO_3$ Bdm is likely low, at most 50 wt. ppm.

Several studies showed $\varphi^{Bdm}_{H_2O}$ in Fe, Al-bearing Bdm is significantly higher than in pure $MgSiO_3$ Bdm[140,141,144,146]. This is attributed to the coupling of H^+ with Al^{3+} to substitute Si^{4+} in the B-site, forming $[Mg^{2+}]_A[Al^{3+}H^+]_BO^{2-}$[42]. The majority of studies[42,141,142,144] reported relatively high values, such as 1000 wt. ppm H_2O in Fe, Al-bearing Bdm, although Liu et al. reported only 10~30 wt. ppm H_2O.

Outlook

Determining Bdm chemistry with high reliability is crucial, as it is the most abundant mineral in Earth's interior. Two high P-T apparatuses are commonly used for studying Bdm chemistry: LH-DAC and MAP. Each has its limitations: LH-DAC can cover the entire P-T range of the lower mantle but produces less reliable results, while MAP yields more reliable results but has limited P-T coverage. To address these issues, efforts should focus on improving the reliability of LH-DAC experiments and extending the P-T range of MAP experiments. It is recommended that future studies investigate the compositions of Bdm coexisting with Fper in the MgO-FeO-Fe_2O_3-Al_2O_3-SiO_2 system as a function of pressure at Known f_{O_2} using these advanced experimental techniques.

Received: 20 May 2024; Accepted: 6 December 2024;
Published online: 01 February 2025

References

1. McDonough, W. F. & Sun, S. S. The composition of the Earth. *Chem. Geol.* **120**, 223–253 (1995).
2. Stixrude, L. & Lithgow-Bertelloni, C. Geophysics of chemical heterogeneity in the mantle. In: Jeanloz, R. (Ed.), *Ann. Rev. Earth Planet. Sci*. **40**, 569–595 (2012).
3. Murakami, M., Hirose, K., Kawamura, K., Sata, N. & Ohishi, Y. Postperovskite phase transition in $MgSiO_3$. *Science* **304**, 855–858 (2004).
4. Zhang, B. H. & Xia, Q. K. Influence of water on the physical properties of olivine, wadsleyite, and ringwoodite. *Eur. J. Mineral.* **33**, 39–75 (2021).
5. Tateno, S., Hirose, K., Sata, N. & Ohishi, Y. Determination of postperovskite phase transition boundary up to 4400 K and implications for thermal structure in D "layer. *Earth Planet. Sci. Lett*. **277**, 130–136 (2009).
6. Fischer, R. A. et al. Equations of state and phase boundary for stishovite and $CaCl_2$-type SiO_2. *Am. Miner.* **103**, 792–802 (2018).
7. Murakami, M., Hirose, K., Ono, S. & Ohishi, Y. Stability of $CaCl_2$-type and α-PbO_2-type SiO_2 at high pressure and temperature determined by in-situ X-ray measurements. *Geophys. Res. Lett.* **30**, 1207 (2003).
8. Dorfman, S. M., Meng, Y., Prakapenka, V. B. & Duffy, T. S. Effects of Fe-enrichment on the equation of state and stability of (Mg,Fe)SiO_3 perovskite. *Earth Planet. Sci. Lett.* **361**, 249–257 (2013).
9. Kobayashi, Y. et al. Fe-Mg partitioning between (Mg, Fe)SiO_3 postperovskite, perovskite, and magnesiowustite in the Earth's lower mantle. *Geophys. Res. Lett.* **32**, L19301 (2005).
10. Sakai, T. et al. Fe-Mg partitioning between perovskite and ferropericlase in the lower mantle. *Am. Miner.* **94**, 921–925 (2009).
11. Ko, B. et al. Calcium dissolution in bridgmanite in the Earth's deep mantle. *Nature* **611**, 88–92 (2022).
12. Shim, S. H. et al. Stability of ferrous-iron-rich bridgmanite under reducing midmantle conditions. *Proc. Natl. Acad. Sci. USA.* **114**, 6468–6473 (2017).
13. Sinmyo, R. & Hirose, K. The Soret diffusion in laser-heated diamond-anvil cell. *Phys. Earth Planet. Inter.* **180**, 172–178 (2010).
14. Moy, A., Fournelle, J. H. & von der Handt, A. Solving the iron quantification problem in low-kV EPMA: an essential step toward improved analytical spatial resolution in electron probe microanalysis-Olivines. *Am. Miner.* **104**, 1131–1142 (2019).
15. Katsura, T. et al. Post-spinel transition in Mg_2SiO_4 determined by high P-T in situ X-ray diffractometry. *Phys. Earth Planet. Inter.* **136**, 11–24 (2003).
16. Ishii, T. et al. Buoyancy of slabs and plumes enhanced by curved post-garnet phase boundary. *Nat. Geosci.* **16**, 828–832 (2023).
17. Ishii, T. et al. Complete agreement of the post-spinel transition with the 660-km seismic discontinuity. *Sci. Rep.* **8**, 6358 (2018).
18. Ishii, T. et al. Sharp 660-km discontinuity controlled by extremely narrow binary post-spinel transition. *Nat. Geosci*. https://doi.org/10.1038/s41561-019-0452-1 (2019).
19. Asahara, Y. et al. Formation of metastable cubic-perovskite in high-pressure phase transformation of Ca(Mg, Fe, Al)Si_2O_6. *Am. Miner.* **90**, 457–462 (2005).
20. Fei, H., Liu, Z., McCammon, C. & Katsura, T. Oxygen vacancy substitution linked to ferric iron in bridgmanite at 27 GPa. *Geophys. Res. Lett.* **47**, e2019GL086296 (2020).
21. Liu, Z. et al. Stability and solubility of the $FeAlO_3$ component in bridgmanite at uppermost lower mantle conditions. *J. Geophys. Res. Solid Earth* **125**, e2019JB018447 (2020).
22. Liu, Z. et al. Aluminum solubility in bridgmanite up to 3000 K at the top lower mantle. *Geosci. Front.* **12**, 929–935 (2021).
23. Wang, L., Liu, Z., Koizumi, S., Boffa Ballaran, T. & Katsura, T. Aluminum components in bridgmanite coexisting with corundum and CF-phase with temperature. *J. Geophys. Res. Solid Earth* **128**, e2022JB025739 (2023).
24. Liu, Z. et al. A new $(Mg_{0.5}Fe^{3+}_{0.5})(Si_{0.5}Al^{3+}_{0.5})O_3$ $LiNbO_3$-type phase synthesized at lower mantle conditions. *Am. Miner.* **104**, 1223–1216 (2019).
25. Ishii, T., McCammon, C. & Katsura, T. Iron and aluminum substitution mechanism in the perovskite phase in the system $MgSiO_3$-$FeAlO_3$-MgO. *Am. Miner.* **108**, 738–743 (2023).

26. Wang, F. et al. A decrease in the $Fe^{3+}/\sum Fe$ ratio of bridgmanite with temperature at the top of the lower mantle. *Earth Planet. Sci. Lett.* **624**, 118440 (2023).
27. Lauterbach, S., McCammon, C. A., van Aken, P., Langenhorst, F. & Seifert, F. Mossbauer and ELNES spectroscopy of (Mg,Fe)(Si,Al)O_3 perovskite: a highly oxidised component of the lower mantle. *Contrib. Mineral. Petrol.* **138**, 17–26 (2000).
28. Frost, D. J. Fe^{2+}-Mg partitioning between garnet, magnesiowustite, and $(Mg,Fe)_2SiO_4$ phases of the transition zone. *Am. Miner.* **88**, 387–397 (2003).
29. Grüninger, H. et al. Oxygen vacancy ordering in aluminous bridgmanite in the Earth's lower mantle. *Geophys. Res. Lett*. **46** https://doi.org/10.1029/2019GL083613 (2019).
30. Chanyshev, A. et al. Ferric Iron Substitution Mechanism in Bridgmanite under SiO_2-Saturated Conditions at 27 GPa. *ACS Earth Space Chem* **7**, 471–478 (2023).
31. Ishii, T. et al. High pressure-temperature phase relations of basaltic crust up to mid-mantle conditions. *Earth Planet. Sci. Lett.* **584**, 117472 (2022).
32. Liu, L. Post-oxide phases of forsterite and enstatite. *Geophys. Res. Lett.* **2**, 417–419 (1975).
33. Horiuchi, H., Ito, E. & Weidner, D. J. Perovskite-type $MgSiO_3$ - single-crystal X-ray-diffraction study. *Am. Miner.* **72**, 357–360 (1987).
34. Tschauner, O. et al. Discovery of davemaoite, $CaSiO_3$-perovskite, as a mineral from the lower mantle. *Science* **374**, 891–894 (2021).
35. Akaogi, M. High-pressure silicates and oxides: phase transition and thermodynamics. Springer Singapore, 206. https://doi.org/10.1007/978-981-19-6363-6 (2022).
36. Shannon, R. D. Revised effective ionic radii and systematic studies of interatomic distances in halides and chalcogenides. *Acta Crystallogr. A* **32**, 751–767 (1976).
37. Liu, Z. D. et al. Phase relations in the system $MgSiO_3$-Al_2O_3 up to 52 GPa and 2000 K. *Phys. Earth Planet. Inter.* **257**, 18–27 (2016).
38. Liu, Z. D., Ballaran, T. B., Huang, R., Frost, D. J. & Katsura, T. Strong correlation of oxygen vacancies in bridgmanite with Mg/Si ratio. *Earth Planet. Sci. Lett.* **523**, 10 (2019).
39. Sano-Furukawa, A., Kuribayashi, T., Komatsu, K., Yagi, T. & Ohtani, E. Investigation of hydrogen sites of wadsleyite: a neutron diffraction study. *Phys. Earth Planet. Inter.* **189**, 56–62 (2011).
40. Ross, N. L., Gibbs, G. V. & Rosso, K. M. Potential docking sites and positions of hydrogen in high-pressure silicates. *Am. Miner.* **88**, 1452–1459 (2003).
41. Townsend, J. P., Tsuchiya, J., Bina, C. R. & Jacobsen, S. D. First-principles investigation of hydrous postperovskite. *Phys. Earth Planet. Int.* **244**, 42–48 (2015).
42. Purevjav, N. et al. Hydrogen incorporation mechanism in the lower-mantle bridgmanite. *Am. Miner.* **109**, 1036–1044 (2024).
43. Ito, E. & Takahashi, E. Postspinel transformations in the system Mg_2SiO_4-Fe_2SiO_4 and some geophysical implications. *J. Geophys. Res. Solid Earth* **94**, 10637–10646 (1989).
44. Kato, T. et al. In situ X ray observation of high-pressure phase transitions of $MgSiO_3$ and thermal expansion of $MgSiO_3$ perovskite at 25 GPa by double-stage multianvil system. *J. Geophys. Res. Solid Earth* **100**, 20475–20481 (1995).
45. Kuroda, K. et al. Determination of the phase boundary between ilmenite and perovskite in $MgSiO_3$ by in situ X-ray diffraction and quench experiments. *Phys. Chem. Miner.* **27**, 523–532 (2000).
46. Ono, S. et al. In situ observation of ilmenite-perovskite phase transition in $MgSiO_3$ using synchrotron radiation. *Geophys. Res. Lett.* **28**, 835–838 (2001).
47. Hirose, K., Komabayashi, T., Murakami, M. & Funakoshi, K. In situ measurements of the majorite-akimotoite-perovskite phase transition boundaries in $MgSiO_3$. *Geophys. Res. Lett.* **28**, 4351–4354 (2001).
48. Ishii, T., Kojitani, H. & Akaogi, M. Post-spinel transitions in pyrolite and Mg_2SiO_4 and akimotoite–perovskite transition in $MgSiO_3$: Precise comparison by high-pressure high-temperature experiments with multi-sample cell technique. *Earth Planet. Sci. Lett.* **309**, 185–197 (2011).
49. Chanyshev, A. et al. Depressed 660-km discontinuity caused by akimotoite–bridgmanite transition. *Nature* **601**, 69–73 (2022).
50. Hernandez, J. A. et al. Direct observation of shock-induced disordering of enstatite below the melting temperature. *Geophys. Res. Lett.* **47**, e2020GL088887 (2020).
51. Yu, Y., Wentzcovitch, R. M., Vinograd, V. L. & Angel, R. J. Thermodynamic properties of $MgSiO_3$ majorite and phase transitions near 660 Km depth in $MgSiO_3$ and Mg_2SiO_4: a first principles study. *J. Geophys. Res. Solid Earth* **116**, B02208 (2011).
52. Ito, E. & Yamada, H. Stability relations of silicate spinels, ilmenites, and perovskites. In: *High*-pressure research in geophys*ics*, 405–419 (1982).
53. Ono, S. & Oganov, A. In situ observations of phase transition between perovskite and $CaIrO_3$-type phase in $MgSiO_3$ and pyrolitic mantle composition. *Earth Planet. Sci. Lett.* **236**, 914–932 (2005).
54. Catalli, K., Shim, S. H. & Prakapenka, V. Thickness and Clapeyron slope of the postperovskite boundary. *Nature* **462**, 782–786 (2009).
55. Tsuchiya, T., Tsuchiya, J., Umemoto, K. & Wentzcovitch, R. A. Phase transition in $MgSiO_3$ perovskite in the earth's lower mantle. *Earth Planet. Sci. Lett.* **224**, 241–248 (2004).
56. Ito, E., Katsura, T. Melting of ferromagnesian silicates under the lower mantle conditions. *In*: Syono, Y., Manghnani, M. H. (Eds.), *High-pressure research: application to earth and planetary sciences*, 315–322. https://doi.org/10.1029/GM067p0315 (1992).
57. Zerr, A. & Boehler, R. Melting of (Mg, Fe)SiO_3-perovskite to 625 Kilobars: indication of a high melting temperature in the lower mantle. *Science* **262**, 553–555 (1993).
58. Shen, G. Y. & Lazor, P. Measurement of melting temperatures of some minerals under lower mantle pressures. *J. Geophys. Res. Solid Earth* **100**, 17699–17713 (1995).
59. Akins, J. A., Luo, S. N., Asimow, P. D. & Ahrens, T. J. Shock-induced melting of $MgSiO_3$ perovskite and implications for melts in Earth's lowermost mantle -: art. no. L14612. *Geophys. Res. Lett.* **31**, L14612 (2004).
60. Mosenfelder, J. L., Asimow, P. D., Frost, D. J., Rubie, D. C. & Ahrens, T. J. The $MgSiO_3$ system at high pressure: thermodynamic properties of perovskite, postperovskite, and melt from global inversion of shock and static compression data. *J. Geophys. Res. Solid Earth* **114**, B01203 (2009).
61. de Koker, N. & Stixrude, L. Self-consistent thermodynamic description of silicate liquids, with application to shock melting of MgO periclase and $MgSiO_3$ perovskite. *Geophys. J. Int.* **178**, 162–179 (2009).
62. Di Paola, C. & Brodholt, J. P. Modeling the melting of multicomponent systems: the case of $MgSiO_3$ perovskite under lower mantle conditions. *Sci Rep-Uk* **6**, 29830 (2016).
63. Liebske, C. & Frost, D. J. Melting phase relations in the MgO–$MgSiO_3$ system between 16 and 26GPa: implications for melting in Earth's deep interior. *Earth Planet. Sci. Lett.* **345-348**, 159–170 (2012).
64. Pierru, R. et al. Solidus melting of pyrolite and bridgmanite: Implication for the thermochemical state of the Earth's interior. *Earth Planet. Sci. Lett.* **595**, 117770 (2022).
65. Irifune, T. et al. The postspinel phase boundary in Mg_2SiO_4 determined by in situ x-ray diffraction. *Science* **279**, 1698–1700 (1998).
66. Fei, Y. et al. Experimentally determined postspinel transformation boundary in Mg_2SiO_4 using MgO as an internal pressure standard and its geophysical implications. *J. Geophys. Res. Solid Earth* **109**, B02305 (2004).

67. Ghosh, S. et al. Effect of water in depleted mantle on post-spinel transition and implication for 660 Km seismic discontinuity. *Earth Planet. Sci. Lett.* **371**, 103–111 (2013).
68. Tsujino, N. et al. Phase transition of wadsleyite-ringwoodite in the Mg_2SiO_4-Fe_2SiO_4 system. *Am. Miner.* **104**, 588–594 (2019).
69. Yao, J., Frost, D. J. & Steinle-Neumann, G. Lower mantle melting: experiments and thermodynamic modeling in the system MgO-SiO_2. *J. Geophys. Res. Solid Earth* **126**, e2021JB022568 (2021).
70. Frost, D. J. & McCammon, C. A. The redox state of Earth's mantle. *Ann. Rev. Earth Planet. Sci.* **36**, 389–420 (2008).
71. McCammon, C. Perovskite as a possible sink for ferric iron in the lower mantle. *Nature* **387**, 694–696 (1997).
72. Liu, L. G. Orthorhombic perovskite phases observed in olivine, pyroxene and garnet at high pressures and temperatures. *Phys. Earth Planet. Inter.* **11**, 289–298 (1976).
73. Kudoh, Y., Prewitt, C. T., Finger, L. W., Darovskikh, A. & Ito, E. Effect of Iron on the crystal-structure of (Mg,Fe)SiO_3 perovskite. *Geophys. Res. Lett.* **17**, 1481–1484 (1990).
74. Ito, E., Takahashi, E. & Matsui, Y. The mineralogy and chemistry of the lower mantle: an implication of the ultrahigh-pressure phase relations in the system MgO-FeO-SiO_2. *Earth Planet. Sci. Lett.* **67**, 238–248 (1984).
75. Fei, Y. W., Wang, Y. B. & Finger, L. W. Maximum solubility of FeO in (Mg, Fe)SiO_3-perovskite as a function of temperature at 26 GPa: Implication for FeO content in the lower mantle. *J. Geophys. Res. Solid Earth* **101**, 11525–11530 (1996).
76. Tange, Y., Takahashi, E., Nishihara, Y., Funakoshi, K.I. & Sata, N. Phase relations in the system MgO-FeO-SiO_2 to 50 GPa and 2000 degrees C: an application of experimental techniques using multianvil apparatus with sintered diamond anvils. *J. Geophys. Res. Solid Earth* **114**, B02214 (2009).
77. Arimoto, T. et al. Phase relations of $MgSiO_3$-$FeSiO_3$ system up to 64 GPa and 2300 K using multianvil apparatus with sintered diamond anvils. *Phys. Earth Planet. Inter.* **295**, 106297 (2019).
78. Mao, H.-K., Shen, G. & Hemley, R. J. Multivariable dependence of Fe-Mg partitioning in the lower mantle. *Science* **278**, 2098–2100 (1997).
79. Lin, J.-F., Speziale, S., Mao, Z. & Marquardt, H. Effects of the electronic spin transitions of iron in lower mantle minerals: implications for deep mantle geophysics and geochemistry. *Rev. Geophys.* **51**, 244–275 (2013).
80. Yoshino, T., Kamada, S., Zhao, C., Ohtani, E. & Hirao, N. Electrical conductivity model of Al-bearing bridgmanite with implications for the electrical structure of the Earth's lower mantle. *Earth Planet. Sci. Lett.* **434**, 208–219 (2016).
81. Huang, R. et al. The composition and redox state of bridgmanite in the lower mantle as a function of oxygen fugacity. *Geochim. Cosmochim. Acta* **303**, 110–136 (2021).
82. Katsura, T. & Ito, E. Determination of Fe-Mg partitioning between perovskite and magnesiowustite. *Geophys. Res. Lett.* **23**, 2005–2008 (1996).
83. Martinez, I., Wang, Y. B., Guyot, F., Liebermann, R. C. & Doukhan, J. C. Microstructures and iron partitioning in (Mg,Fe)SiO_3 perovskite (Mg,Fe)O magnesiowustite assemblages: an analytical transmission electron microscopy study. *J. Geophys. Res. Solid Earth* **102**, 5265–5280 (1997).
84. Frost, D. J. & Langenhorst, F. The effect of Al_2O_3 on Fe-Mg partitioning between magnesiowustite and magnesium silicate perovskite. *Earth Planet. Sci. Lett.* **199**, 227–241 (2002).
85. Nakajima, Y., Frost, D. J. & Rubie, D. C. Ferrous iron partitioning between magnesium silicate perovskite and ferropericlase and the composition of perovskite in the Earth's lower mantle. *J. Geophys. Res. Solid Earth* **117**, 12 (2012).
86. Andrault, D. Evaluation of (Mg,Fe) partitioning between silicate perovskite and magnesiowustite up to 120 GPa and 2300K. *J. Geophys. Solid Earth* **106**, 2079–2087 (2001).
87. Kesson, S. E., Fitz Gerald, J. D., O'Neill, H. S. & Shelley, J. M. G. Partitioning of iron between magnesian silicate perovskite and magnesiowiistite at about 1 Mbar. *Phys. Earth Planet. Inter.* **131**, 295–310 (2002).
88. Auzende, A. L. et al. Element partitioning between magnesium silicate perovskite and ferropericlase: new insights into bulk lower-mantle geochemistry. *Earth Planet. Sci. Lett.* **269**, 164–174 (2008).
89. Sinmyo, R. et al. Partitioning of iron between perovskite/postperovskite and ferropericlase in the lower mantle. *J. Geophys. Res. Solid Earth* **113**, B11204 (2008).
90. Nomura, R., Zhou, Y. & Irifune, T. Melting phase relations in the $MgSiO_3$–$CaSiO_3$ system at 24 GPa. *Prog. Earth Planet. Sci.* **4**, 34 (2017).
91. Corgne, A., Liebske, C., Wood, B. J., Rubie, D. C. & Frost, D. J. Silicate perovskite-melt partitioning of trace elements and geochemical signature of a deep perovskitic reservoir. *Geochim. Cosmochim. Acta* **69**, 485–496 (2005).
92. Irifune, T., Susaki, J., Yagi, T. & Sawamoto, H. Phase-transformations in diopside $CaMgSi_2O_6$ at pressures up to 25 GPa. *Geophys. Res. Lett.* **16**, 187–190 (1989).
93. Irifune, T., Susaki, J., Yagi, T. & Sawamoto, H. High-pressure phase transformation in $CaMgSi_2O_6$ and implications for origin of ultra-deep diamond inclusions. *Geophys. Res. Lett*. **27**, 3541–3544 (2000).
94. Creasy, N., Girard, J., Eckert, J. O. & Lee, K. K. M. The Role of redox on bridgmanite crystal chemistry and calcium speciation in the lower mantle. *J. Geophys. Res. Solid Earth* **125**, e2020JB020783 (2020).
95. Liu, L. G. Silicate perovskite from phase transformations of pyrope-garnet at high pressure and temperature. *Geophys. Res. Lett.* **1**, 277–280 (1974).
96. Liu, L. G. High-pressure reconnaissance investigation in the system $Mg_3Al_2Si_3O_{12}$-$Fe_3Al_2Si_3O_{12}$. *Earth Planet. Sci. Lett.* **26**, 425–433 (1975).
97. Liu, L.-G. The system enstatite-pyrope at high pressures and temperatures and the mineralogy of the Earth's mantle. *Earth Planet. Sci. Lett.* **36**, 237–245 (1977).
98. Irifune, T., Koizumi, T. & Ando, J. I. An experimental study of the garnet-perovskite transformation in the system $MgSiO_3$-$Mg_3Al_2Si_3O_{12}$. *Phys. Earth Planet. Inter.* **96**, 147–157 (1996).
99. Akaogi, M. & Ito, E. Calorimetric study on majorite-perovskite transition in the system $Mg_4Si_4O_{12}$-$Mg_3Al_2Si_3O_{12}$: transition boundaries with positive pressure-temperature slopes. *Phys. Earth Planet. Inter.* **114**, 129–140 (1999).
100. Kubo, A. & Akaogi, M. Post-garnet transitions in the system $Mg_4Si_4O_{12}$-$Mg_3Al_2Si_3O_{12}$ up to 28 GPa: phase relations of garnet, ilmenite and perovskite. *Phys. Earth Planet. Inter.* **121**, 85–102 (2000).
101. Hirose, K., Fei, Y. W., Ono, S., Yagi, T. & Funakoshi, K. In situ measurements of the phase transition boundary in $Mg_3Al_2Si_3O_{12}$: implications for the nature of the seismic discontinuities in the Earth's mantle. *Earth Planet. Sci. Lett.* **184**, 567–573 (2001).
102. Akaogi, M., Tanaka, A. & Ito, E. Garnet-ilmenite-perovskite transitions in the system $Mg_4Si_4O_{12}$-$Mg_3Al_2Si_3O_{12}$ at high pressures and high temperatures: phase equilibria, calorimetry and implications for mantle structure. *Phys. Earth Planet. Inter.* **132**, 303–324 (2002).
103. Navrotsky, A. et al. Aluminum in magnesium silicate perovskite: formation, structure, and energetics of magnesium-rich defect solid solutions. *J. Geophys. Res. Solid Earth* **108**, 2330 (2003).

104. Yamamoto, T., Yuen, D. A. & Ebisuzaki, T. Substitution mechanism of Al ions in $MgSiO_3$ perovskite under high pressure conditions from first-principles calculations. *Earth Planet. Sci. Lett.* **206**, 617–625 (2003).
105. Akber-Knutson, S. & Bukowinski, M. S. T. The energetics of aluminum solubility into $MgSiO_3$ perovskite at lower mantle conditions. *Earth Planet. Sci. Lett.* **220**, 317–330 (2004).
106. Panero, W. R., Akber-Knutson, S. & Stixrude, L. Al_2O_3 incorporation in $MgSiO_3$ perovskite and ilmenite. *Earth Planet. Sci. Lett.* **252**, 152–161 (2006).
107. Walter, M. J. et al. Subsolidus phase relations and perovskite compressibility in the system MgO-$AlO_{1.5}$-SiO_2 with implications for Earth's lower mantle. *Earth Planet. Sci. Lett.* **248**, 77–89 (2006).
108. Tsuchiya, J. & Tsuchiya, T. Postperovskite phase equilibria in the $MgSiO_3$-Al_2O_3 system. *Proc. Natl. Acad. Sci. USA.* **105**, 19160–19164 (2008).
109. Ishii, T. et al. Synthesis and crystal structure of $LiNbO_3$-type $Mg_3Al_2Si_3O_{12}$: a possible indicator of shock conditions of meteorites. *Am. Miner.* **102**, 1947–1952 (2017).
110. Liu, Z.-D., Ishii, T. & Katsura, T. Rapid decrease in oxygen-vacancy substitution in aluminous bridgmanite with pressure. *Geochem. Persp. Lett.* **5**, 12–18 (2017).
111. Irifune, T., Fujino, K. & Ohtani, E. A new high-pressure form of $MgAl_2O_4$. *Nature* **349**, 409–411 (1991).
112. Ishii, T. et al. High-pressure phase relations and crystal structures of postspinel phases in MgV_2O_4, FeV_2O_4, and $MnCr_2O_4$: Crystal chemistry of AB_2O_4 postspinel compounds. *Inorg. Chem.* **57**, 6648–6657 (2018c).
113. Kojitani, H., Hisatomi, R. & Akaogi, M. High-pressure phase relations and crystal chemistry of calcium ferrite-type solid solutions in the system $MgAl_2O_4$-Mg_2SiO_4. *Am. Miner.* **92**, 1112–1118 (2007).
114. Liu, Z. et al. Phase relations in the system $MgSiO_3$–Al_2O_3 up to 2300 K at lower-mantle pressures. *J. Geophys. Res. Solid Earth* **122**, 7775–7788 (2017).
115. Muir, J. M. R., Thomson, A. R. & Zhang, F. W. The miscibility of calcium silicate perovskite and bridgmanite: a single perovskite solid solution in hot, iron-rich regions. *Earth Planet. Sci. Lett.* **566**, 10 (2021).
116. Funamori, N. & Jeanloz, R. High-pressure transformation of Al_2O_3. *Science* **278**, 1109–1111 (1997).
117. Hirsch, L. M. & Shankland, T. J. Point-defects in $(Mg,Fe)SiO_3$ perovskite. *Geophys. Res. Lett.* **18**, 1305–1308 (1991).
118. Kojitani, H., Katsura, T. & Akaogi, M. Aluminum substitution mechanisms in perovskite-type $MgSiO_3$: an investigation by Rietveld analysis. *Phys. Chem. Miner.* **34**, 257–267 (2007).
119. Liu, Z., Akaogi, M. & Katsura, T. Increase of the oxygen vacancy component in bridgmanite with temperature. *Earth Planet. Sci. Lett.* **505**, 141–151 (2019).
120. Stebbins, J. F., Kojitani, H., Akaogi, M. & Navrotsky, A. Aluminum substitution in $MgSiO_3$ perovskite: investigation of multiple mechanisms by Al-27 NMR. *Am. Miner.* **88**, 1161–1164 (2003).
121. Stebbins, J. F. et al. Aluminum substitution in stishovite and $MgSiO_3$ perovskite: high-resolution Al-27 NMR. *Am. Miner.* **91**, 337–343 (2006).
122. Hummer, D. R. & Fei, Y. Synthesis and crystal chemistry of Fe^{3+}-bearing $(Mg,Fe^{3+})(Si,Fe^{3+})O_3$ perovskite. *Am. Miner.* **97**, 1915–1921 (2012).
123. Fei, H. et al. Pressure destabilizes oxygen vacancies in bridgmanite. *J. Geophys. Res. Solid Earth* **126**, e2021JB022437 (2021).
124. Bykova, E. et al. Structural complexity of simple Fe2O3 at high pressures and temperatures. *Nat. Commun.* **7**, 10661 (2016).
125. Huang, R. et al. The Effect of Fe-Al substitution on the crystal Structure of $MgSiO_3$ bridgmanite. *J. Geophys. Res. Solid Earth* **126**, e2021JB021936 (2021).
126. Nishio-Hamane, D., Nagai, T., Fujino, K., Seto, Y. & Takafuji, N. Fe^{3+} and Al solubilities in $MgSiO_3$ perovskite: implication of the $Fe^{3+}AlO_3$ substitution in $MgSiO_3$ perovskite at the lower mantle condition. *Geophys. Res. Lett.* **32**, L16306 (2005).
127. Boffa Ballaran, T. et al. Effect of chemistry on the compressibility of silicate perovskite in the lower mantle. *Earth Planet. Sci. Lett.* **333–334**, 181–190 (2012).
128. Sinmyo, R., Hirose, K., Muto, S., Ohishi, Y. & Yasuhara, A. The valence state and partitioning of iron in the Earth's lowermost mantle. *J. Geophys. Res.* **116**, B07205 (2011).
129. Prescher, C., Langenhorst, F., Dubrovinsky, L. S., Prakapenka, V. B. & Miyajima, N. The effect of Fe spin crossovers on its partitioning behavior and oxidation state in a pyrolitic Earth's lower mantle system. *Earth Planet. Sci Lett.* **399**, 86–91 (2014).
130. Piet, H. et al. Spin and valence dependence of iron partitioning in Earth's deep mantle. *Proc. Natl. Acad. Sci. USA.* **113**, 11127–11130 (2016).
131. Irifune, T. et al. Iron partitioning and density changes of pyrolite in Earth's lower mantle. *Science* **327**, 193–195 (2010).
132. Stixrude, L. & Lithgow-Bertelloni, C. Thermal expansivity, heat capacity and bulk modulus of the mantle. *Geophys. J. Int.* **228**, 1119–1149 (2022).
133. Stixrude, L. & Lithgow-Bertelloni, C. Thermodynamics of mantle minerals - II. Phase equilibria. *Geophys. J. Int.* **184**, 1180–1213 (2011).
134. Katsura, T. & Tange, Y. A simple derivation of the Birch–Murnaghan equations of state (EOSs) and comparison with EOSs derived from other definitions of finite strain. *Miner* **9**, 745 (2019).
135. Poierier, J. P. Introduction to the Physics of the Earth's Interior, 2nd edition. Cambridge University Press, Cambridge, 328. https://doi.org/10.1017/CBO9781139164467 (2012).
136. Frost, D. J. et al. Experimental evidence for the existence of iron-rich metal in the Earth's lower mantle. *Nature* **428**, 409–412 (2004).
137. Frost, D.J. & McCammon, C.A. The redox state of Earth's mantle. *Annu. Rev. Earth Planet. Sci.* **36**, 389–420 (2008).
138. Meade, C., Reffner, J. A. & Ito, E. Synchrotron infrared absorbance measurements of hydrogen in $MgSiO_3$ perovskite. *Science* **264**, 1558–1560 (1994).
139. Murakami, M. et al. Water in Earth's lower mantle. *Science* **295**, 1885–1887 (2002).
140. Bolfan-Casanova, N., Keppler, H. & Rubie, D. C. Water partitioning at 660 Km depth and evidence for very low water solubility in magnesium silicate perovskite. *Geophys. Res. Lett.* **30**, 1905 (2003).
141. Litasov, K. et al. Water solubility in Mg-perovskites and water storage capacity in the lower mantle. *Earth Planet. Sci. Lett.* **211**, 189–203 (2003).
142. Inoue, T., Wada, T., Sasaki, R. & Yurimoto, H. Water partitioning in the Earth's mantle. *Phys. Earth Planet. Int.* **183**, 245–251 (2010).
143. Panero, W. R. et al. Dry $(Mg,Fe)SiO_3$ perovskite in the Earth's lower mantle. *J. Geophys. Res. Solid Earth* **120**, 894–908 (2015).
144. Fu, S. et al. Water concentration in single-crystal (Al,Fe)-bearing bridgmanite grown from the hydrous melt: implications for dehydration melting at the topmost lower mantle. *Geophys. Res. Lett.* **46**, 10346–10357 (2019).
145. Liu, Z. et al. Bridgmanite is nearly dry at the top of the lower mantle. *Earth Planet. Sci. Lett.* **570**, 117088 (2021).
146. Ishii, T., Ohtani, E. & Shatskiy, A. Aluminum and hydrogen partitioning between bridgmanite and high-pressure hydrous phases: implications for water storage in the lower mantle. *Earth Planet. Sci. Lett.* **583**, 117441 (2022).
147. Yang, Y. N. et al. NanoSIMS analysis of water content in bridgmanite at the micron scale: an experimental approach to probe water in Earth's deep mantle. *Front. Chem.* **11**, 1166593 (2023).

148. Hernández, E. R., Alfè, D. & Brodholt, J. The incorporation of water into lower-mantle perovskites: a first-principles study. *Earth Planet. Sci. Lett.* **364**, 37–43 (2013).
149. Ito, E. & Weidner, D. J. Crystal growth of $MgSiO_3$ perovskite. *Geophys. Res. Lett.* **13**, 464–466 (1986).

Acknowledgements

I thank Msasaki Akaogi for producing Fig. 2 and Fei Wang for calculating the Bdm compositions shown in Fig. S1. I acknowledge Christian Liebske and three anonymous reviewers for their helpful comments. This work was funded by a research project approved by the European Research Council (ERC) under the European Union's Horizon 2020 research and innovation program (Proposal no. 787527)

Author contributions

T.K. conducted all scientific work except for preparing Figs. 2 and S1.

Competing interests

The author declares competing interests.

Additional information

Supplementary information The online version contains supplementary material available at https://doi.org/10.1038/s42004-024-01389-8.

Correspondence and requests for materials should be addressed to Tomoo Katsura.

Peer review information *Communications Chemistry* thanks Christian Liebske and the other, anonymous, reviewers for their contribution to the peer review of this work.

Reprints and permissions information is available at http://www.nature.com/reprints

Publisher's note Springer Nature remains neutral with regard to jurisdictional claims in published maps and institutional affiliations.

Open Access This article is licensed under a Creative Commons Attribution-NonCommercial-NoDerivatives 4.0 International License, which permits any non-commercial use, sharing, distribution and reproduction in any medium or format, as long as you give appropriate credit to the original author(s) and the source, provide a link to the Creative Commons licence, and indicate if you modified the licensed material. You do not have permission under this licence to share adapted material derived from this article or parts of it. The images or other third party material in this article are included in the article's Creative Commons licence, unless indicated otherwise in a credit line to the material. If material is not included in the article's Creative Commons licence and your intended use is not permitted by statutory regulation or exceeds the permitted use, you will need to obtain permission directly from the copyright holder. To view a copy of this licence, visit http://creativecommons.org/licenses/by-nc-nd/4.0/.

© The Author(s) 2025, modified publication 2026